

Can crystal morphology indicate different generations of dolomites? Evidence from magnesium isotopes



Meng Ning^a, Kangjun Huang^b, Xianguo Lang^c, Haoran Ma^a, Honglin Yuan^b, Yongbo Peng^d,
Bing Shen^{a,*}

^a Key Laboratory of Orogenic Belts and Crustal Evolution, MOE, School of Earth and Space Sciences, Peking University, Beijing, China

^b State Key Laboratory of Continental Dynamics, Shanxi Key Laboratory of Early Life and Environment, Department of Geology, Northwest University, Xi'an, China

^c State Key Laboratory of Palaeobiology and Stratigraphy, Nanjing Institute of Geology and Palaeontology, Center for Excellence in Life and Paleoenvironment, Chinese Academy of Sciences, Nanjing, China

^d Department of Geology and Geophysics, Louisiana State University, Baton Rouge, LA, USA

ARTICLE INFO

Editor: Dong Hailiang

Keywords:

Dolomitization

Magnesium isotope

Dolomite crystal morphology

Ordovician, Majiagou Formation, North China

ABSTRACT

Among various geochemical and petrographic approaches, dolomite crystal morphology and dolostone fabric have been widely applied in the study of ancient dolostones. It is proposed that dolomite crystal morphologies and the rock fabric may reflect the formation temperature, and thus can be used to distinguish different generations of dolomite. However, this scenario has also been challenged by some researchers. In order to test whether the dolomite crystal morphology can be used to differentiate different generations of dolomite, in this study, we measured the Mg isotopic compositions ($\delta^{26}\text{Mg}$) of dolomite with different crystal morphologies. $\delta^{26}\text{Mg}$ of dolomite is controlled by a variety of factors, including temperature, magnesium isotopic composition of dolomitization fluids, and the flow rate of dolomitization fluids. If dolomite with distinct crystal morphologies were derived from different dolomitization processes, it is highly plausible that they would have different $\delta^{26}\text{Mg}$. Five types of dolomite with distinct crystal morphologies and rock fabric were recognized from three sampling intervals (S1, S2, and S3) in the middle Ordovician Majiagou Formation in North China. Different types of dolomite in the same sampling interval have similar $\delta^{26}\text{Mg}$ values, suggesting that these dolomites might have derived during the same dolomitization event. Our study indicates that the crystal morphology alone may not unambiguously differentiate the generations of dolomites. We propose the following reasons: (1) the dolomite crystal morphology might be controlled by various factors rather than the formation temperature alone, or (2) the dolomite crystal morphology might be modified in diagenesis, but $\delta^{26}\text{Mg}$ remains unchanged.

1. Introduction

Formation of ancient massive dolostones cannot be explained by any dolomitization models that were established based on the studies of modern dolomite (Fairbridge, 1957; Purser et al., 1994; Zenger et al., 1994), which challenges the paradigm of ‘the present is the key to the past’ (Warren, 2000). Ancient dolostones may cover up to hundreds of thousands square kilometers in area, and are hundreds to thousands of meters in thickness (Mresah, 1998; Lumsden and Caudle, 2001). In contrast, modern dolomite is normally discovered as discrete layers of centimeters to meters in thickness, and has limited geographic distributions in specific environments (Purser et al., 1994; Arvidson and Mackenzie, 1999). Moreover, ancient dolostones typically show a highly ordered crystal lattice with Mg/Ca (molar ratio) close to 1 (the

stoichiometric dolomite), while modern dolomites are normally Ca-rich and have low to medium degree of cation order (Kaczmarek and Sibley, 2011; Last et al., 2012; Petrush et al., 2017). Furthermore, modern dolomite is typically precipitated as cements, and is found only rarely as replacive in nature (Petrush et al., 2017). In addition, dolomite minerals cannot easily be inorganically synthesized at room temperature, regardless of the saturation state of the solution (Land, 1998). Thus, although the modern seawater is supersaturated with respect to dolomite, it is proposed that dolomite formation might be prohibited by the energy barrier imposed by the hydration of Mg^{2+} in seawater (Lippmann, 1982; Markham et al., 2002; Machel, 2004) or by seawater/porewater SO_4^{2-} (Slaughter and Hill, 1991).

Traditional methodologies for the study of ancient dolostone include the conventional isotopes (C, O, and Sr isotopes), trace element

* Corresponding author.

E-mail address: bingshen@pku.edu.cn (B. Shen).

geochemistry, and petrographic observations (see reviews by Land, 1980; Sibley and Gregg, 1987; Sibley, 1991; Mazzullo, 1992; Allan and Wiggins, 1993; Warren, 2000; Machel, 2004; Gregg et al., 2015). Among the various canonical approaches, dolomite crystal morphology has been widely applied to distinguish different generations of dolomites (e.g., Mazzullo, 1992; Sachan, 1993; Zheng et al., 1994; Braithwaite et al., 2004; Azmy et al., 2008; Conliffe et al., 2012; Olanipekun et al., 2014). Based on the crystal growth theory, the crystal morphologies, including the crystal size distribution and crystal boundary shape, may reflect a combination of the formation temperature and the saturation state of dolomitization solution (Gregg and Sibley, 1984; Sibley and Gregg, 1987; Sibley, 1991). It is further proposed that the relative rates of nucleation and crystal growth are strongly temperature dependent and determine the crystal boundary shape of dolomite (Sibley, 1991; Mazzullo and Chilingarian, 1996). Therefore, dolomites with different crystal morphologies may be, implicitly, assumed to derive from time-separated phases of dolomitization (Gregg and Sibley, 1984; Taylor and Sibley, 1986; Sibley and Gregg, 1987; Sibley, 1991; Mazzullo, 1992). However, some researchers have also questioned validity of this approach. It is proposed that the dolomite crystal morphology may not always be temperature-dependent, and instead, might be related to the competition for growth space during dolomite formation (Jones, 2005; Jones, 2013). Therefore, whether the dolomite crystal morphology can be used to distinguish different generations of dolomitization needs more rigorous evaluation by novel techniques.

In this study, we approach questions of dolomite morphology with the novel Mg isotope system. Mg is the key element in dolomite. Dolomite formation requires Mg supply and overcoming the energy barrier imposed by Mg²⁺ hydration (Lippmann, 1982; Slaughter and Hill, 1991). With the development of high resolution Multi-Collector Inductively Coupled Plasma Mass Spectrometry (MC-ICP-MS) two decades ago, Mg isotopes have become an important approach in the study of dolomite/dolostone formation, and might provide the direct constraint on the origin of ancient dolostone (Daughtry et al., 1962; Carder et al., 2005a; Carder et al., 2005b; Geske et al., 2012; Azmy et al., 2013; Lavoie et al., 2014; Mavromatis et al., 2014; Blättler et al., 2015; Geske et al., 2015a; Geske et al., 2015b; Huang et al., 2015; Li et al., 2016; Peng et al., 2016; Li et al., 2018). Firstly, Mg isotopes can be used to constrain the Mg source, because major Mg reservoirs in Earth's surface show a wide range of variation in $\delta^{26}\text{Mg}$ (Tipper et al., 2006; Higgins and Schrag, 2010; Li et al., 2010; Tipper et al., 2010; Ling et al., 2011; Wimpenny et al., 2014; Blättler et al., 2015; Schott et al., 2016; Teng, 2017; Wan et al., 2017). Secondly, carbonate mineral (Ca-carbonate and dolomite) formation is associated with significant fractionation in Mg isotopes (Galy et al., 2002; Chang et al., 2004; Buhl et al., 2007; Hippler et al., 2009; Higgins and Schrag, 2010; Immenhauser et al., 2010; Geske et al., 2012; Higgins and Schrag, 2012; Fante and Higgins, 2014; Blättler et al., 2015; Geske et al., 2015a; Geske et al., 2015b), and the fractionation factors for carbonate mineral (including calcite, aragonite, dolomite and magnesite) formation at room temperature have been determined with relatively small uncertainties (Immenhauser et al., 2010; Wombacher et al., 2011; Li et al., 2012; Saulnier et al., 2012; Mavromatis et al., 2013; Fante and Higgins, 2014; Blättler et al., 2015; Li et al., 2015; Wang et al., 2017). More importantly, Mg isotopic composition of dolostone ($\delta^{26}\text{Mgdol}$) is systematically higher (about 2‰) than that of limestone ($\delta^{26}\text{Mglim}$) (Galy et al., 2002; Higgins and Schrag, 2010; Fante and Higgins, 2014; Blättler et al., 2015; Huang et al., 2015). Such systematic differences cannot be explained by the variation of isotopic fractionation alone, but may indicate the distinct processes of dolostone and limestone formation (Huang et al., 2015). In previous studies, two dolomitization models, the advective flow (AF) and the diffusion-advection-reaction (DAR) models have been developed to simulate the Mg isotope systematics during dolostone formation (Huang et al., 2015; Peng et al., 2016), although the actual dolomitization processes are much more

complex. The AF and DAR modeling results indicate that $\delta^{26}\text{Mgdol}$ is affected by a number of factors, including seawater Mg isotopic composition ($\delta^{26}\text{Mg}_{\text{sw}}$), temperature, sedimentation rate, isotopic fractionation during dolomite precipitation (Δ_{dol}), and the rate of dolomite formation (Huang et al., 2015; Peng et al., 2016).

Given the available theoretical frameworks and the precise determination of isotopic fractionation during dolomite precipitation (Huang et al., 2015; Li et al., 2015; Peng et al., 2016), it is timely to reexamine some traditional scenarios of dolomite formation by using Mg isotopes. Because Mg isotopic composition of dolomite could be affected by a number of factors as depicted above, dolomite forming through different phases of dolomitization tend to have different $\delta^{26}\text{Mg}$ values. Thus, $\delta^{26}\text{Mg}$ of dolomites may shed light on distinguishing the generations of dolomitization.

In this study, we measured $\delta^{26}\text{Mg}$ of dolostone samples from the middle Ordovician Majiagou Formation in the North China Block (NCB). On the basis of systematic petrographic analyses, five types of dolomite with distinct crystal morphologies and rock fabric were identified. Then, we used Mg isotopes to test whether the dolomite crystal morphology can uniquely constrain the generation of dolomite. If dolomites with distinct crystal morphologies were derived from different generations of dolomitization, it is highly plausible that their Mg isotopic values would be different.

2. Geological background

Carbonate samples were collected from the middle Ordovician Majiagou Formation in the Seshufen section in the Western Hills of Beijing, NCB (Fig. 1). The NCB was developed as a shallow marine carbonate platform since middle Cambrian (Liu, 1999). Such depositional environment had persisted until late middle Ordovician, when the NCB was uplifted and eroded. The Ordovician succession in the NCB consists of, in ascending order, the Yeli, Liangjiashan and Majiagou formations. The Yeli Formation conformably overlies the late Cambrian Chaomidian Formation, and is mainly composed of ribbon rocks, which consists of alternating cm-thick limestone and marlstone layers (Westphal et al., 2008). The overlying Liangjiashan Formation is characterized by the alternating deposition of medium- to thick-bedded bioturbated limestone and stromatoporoid-bearing limestone with occasional occurrences of intraclastic limestone; and the upper part of the Liangjiashan Formation is partially dolomitized. The beginning of the Majiagou Formation is marked by the deposition of a breccia layer, indicating a depositional hiatus between the Liangjiashan and Majiagou formations (collectively called the Huaiyuan movement, (Tian and Zhang, 1997)) (Fig. 1). The Majiagou Formation is mainly composed of dark gray, thick-bedded dolomitic limestone and dolostone, and is unconformably overlain by the late Carboniferous Qingshuijian (Benxi) Formation. This unconformity can be easily identified by a layer of conglomerates with well sorted and rounded pebbles (Fig. 1).

In the Seshufen section, the Majiagou Formation is about 400 m thick, and can be divided into the lower and upper members (Xie, 1991). In this study, 120 samples were collected from three measured stratigraphic intervals (Fig. 2). The lower sampling interval (S1) is at the top of the lower member, the middle sampling interval (S2) is located near the base of the upper member, while the upper sampling interval (S3) is close to the top of the Majiagou Formation (Fig. 1).

3. Lithofacies and meter-scale cycles

3.1. Lithofacies

On the basis of detailed outcrop description and thin section observation, eight lithofacies can be recognized in the Majiagou Formation (Table A1):

(LT1) Fenestral laminated dolostone (Fig. 3a). This lithofacies is

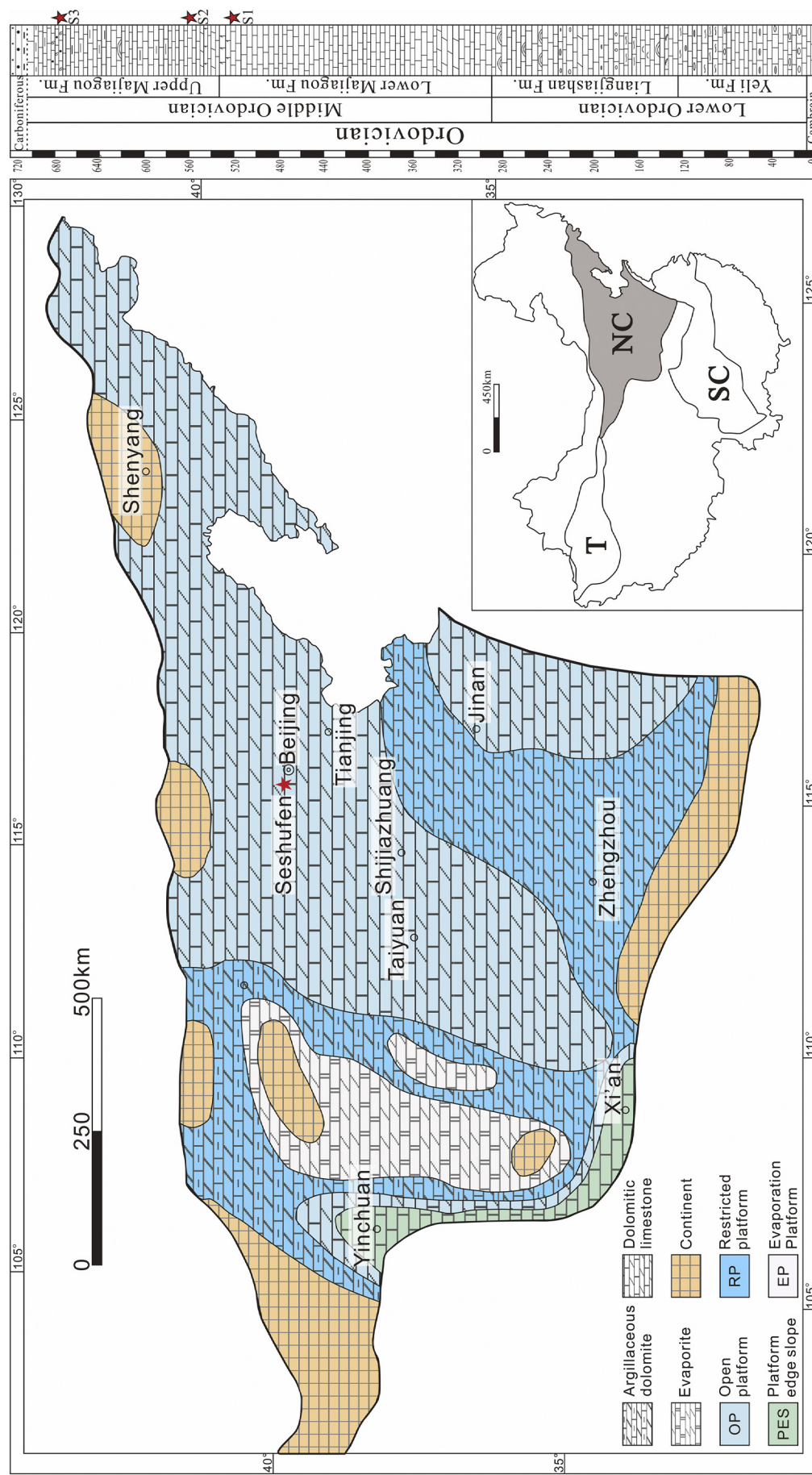


Fig. 1. Middle Ordovician paleogeographic map of the North China Block (left) and the stratigraphic column of idealized Ordovician succession in North China (right) (modified from Chen et al. (2015)). The sampling locality of the Seshufen section (red star) is located southwest of Beijing. (For interpretation of the references to colour in this figure legend, the reader is referred to the web version of this article.)

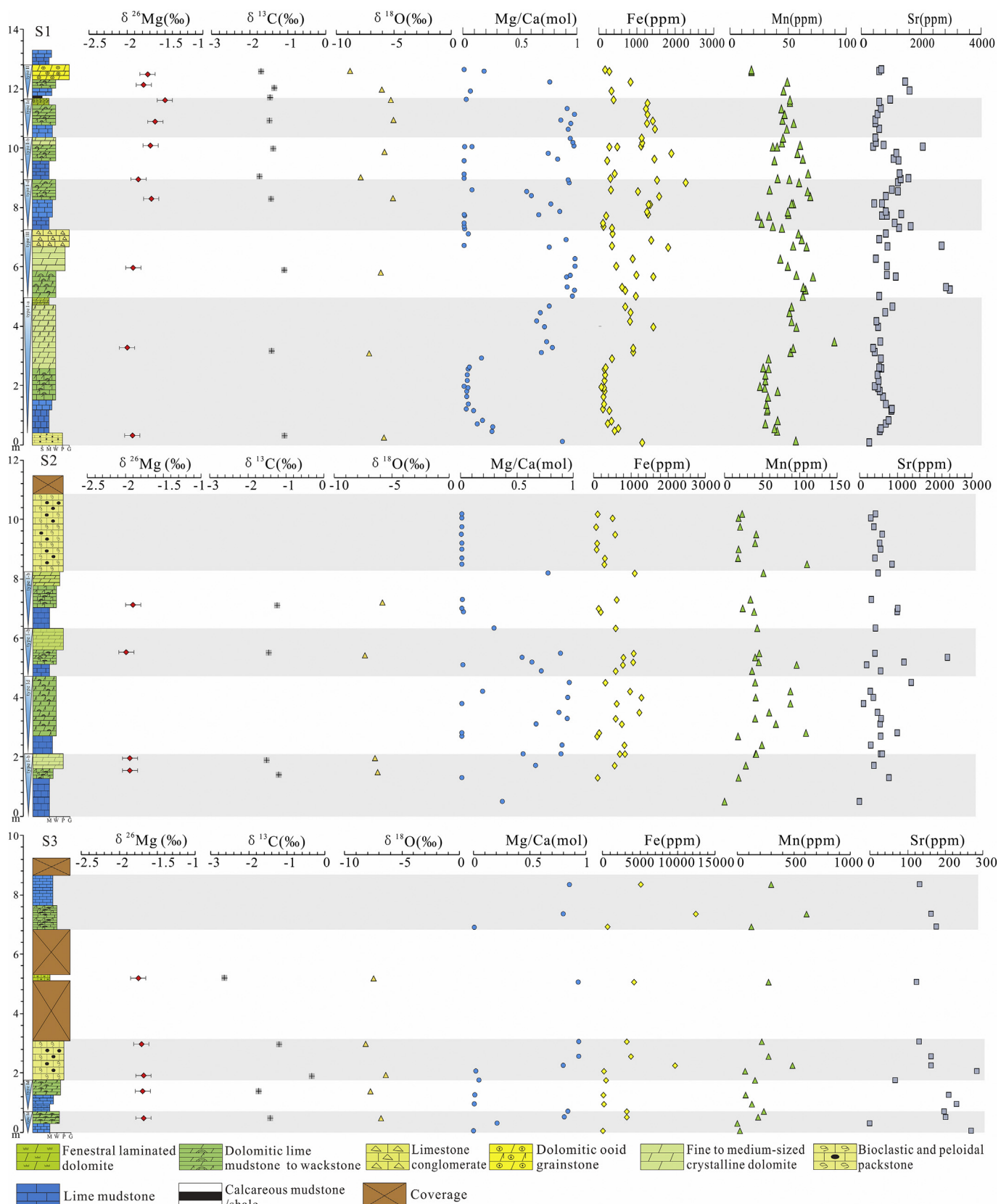
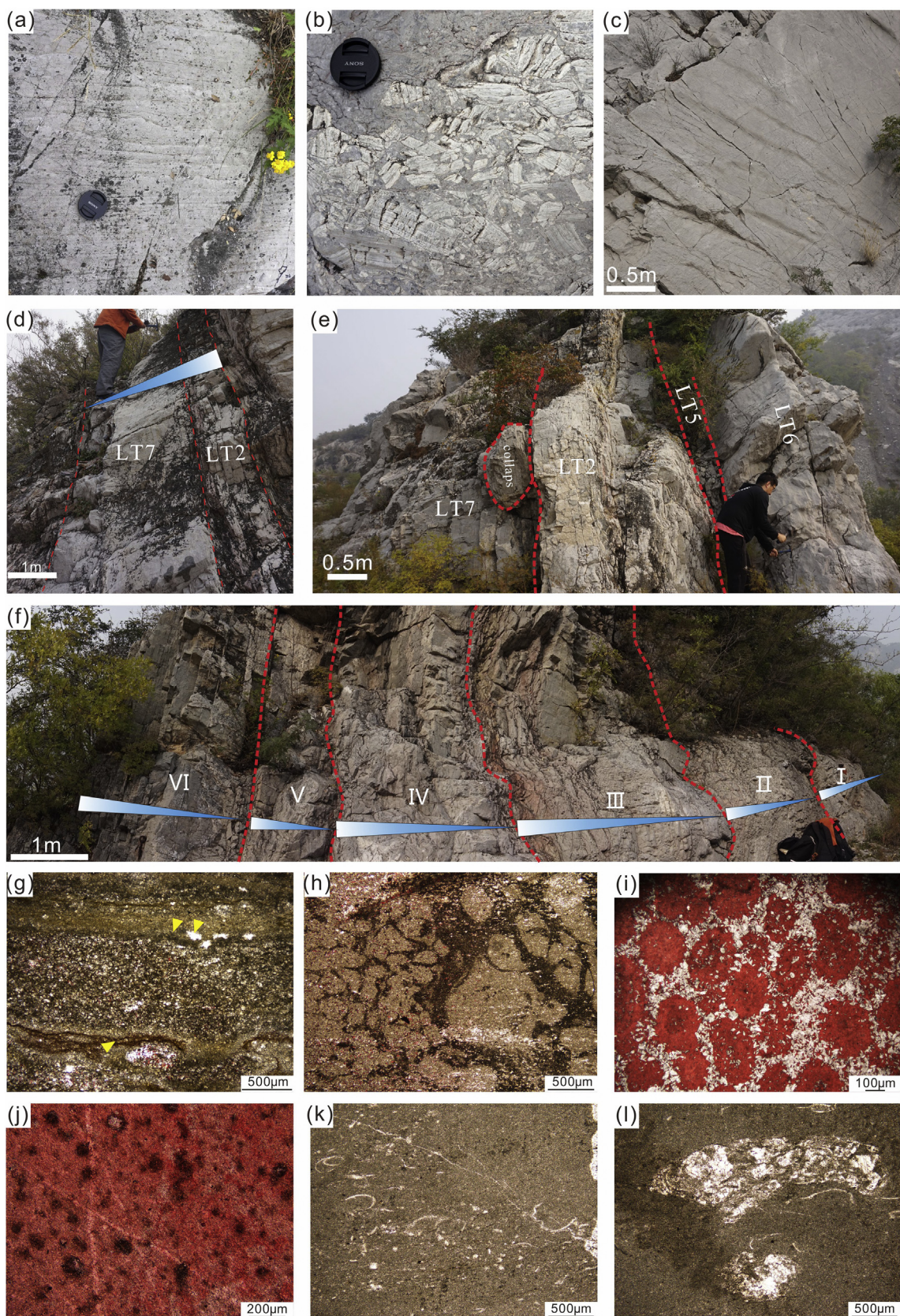


Fig. 2. Stratigraphic profiles of $\delta^{26}\text{Mg}$, $\delta^{13}\text{C}$, $\delta^{18}\text{O}$, Mg/Ca ratio and trace elements (Fe, Mn, Sr) compositions of three sampling intervals (S1, S2, S3) of the Majiagou Formation in the Seshufen section.



(caption on next page)

characterized by pale gray laminated dolomitic with common occurrence of fenestrate structures (Fig. 3g). The fenestral structures commonly indicate a subaerial exposure, and therefore this

lithofacies represents the upper intertidal to supratidal deposition (Davis and Dalrymple, 2012).

(LT2) Dolomitic lime mudstone to wackestone (Fig. 3d). Though

Fig. 3. Field photographs and photomicrographs of the Majiagou Formation in the Seshufen section. (a) Fenestral laminated dolostone (LT1) in S1. (b) Limestone breccia (LT3), showing in situ breakage of laminated dolomite; clasts are composed of autoclastic laminated dolomite and matrices are composed of micrite. (c) Asymmetrical ripple marks in the surface of thick-bedded bioclastic and peloidal packstone (LT6). (d) Thin bedded dolomitic lime mudstone to wackstone (LT2) and thick bedded lime mudstone (LT7) succession in S1. (e) Thick bedded lime mudstone (LT7), thin bedded dolomitic lime mudstone to wackstone (LT2), crystalline dolomite (LT5) and thick bedded bioclastic and peloidal packstone (LT6) succession at the top of S2. (f) 6 shoaling upward cycles in S1 outcrop. (g) Fenestrate structures (yellow arrows) in laminated dolostone facies. (h) Micritic calcified algae fragments retained in dolomitic lime mudstone to wackstone (LT2). (i) Dolomitic ooid grainstone, undolomitized ooids are cemented by crystalline dolomite (unstained). (j) Peloidal packstone (LT6), peloids showing partial dolomitization. (k) Bioclastic packstone (LT6). (l) Bioclastic packstone (LT6) with burrows filled by sparry calcite. (For interpretation of the references to colour in this figure legend, the reader is referred to the web version of this article.)

partially dolomitized, the original rock fabric, such as filiform textures, can still be identified. Clasts are mainly composed of dark, micritic calcified algae fragments (Fig. 3h). This lithofacies represents the deposition at low-energy subtidal to intertidal environments.

(LT3) Limestone breccia (Fig. 3b). This lithofacies is clast-supported and cemented by microcrystalline calcite. The gravels are dominated by unsorted, angular, laminated dolomite fragments and commonly vary from 1 to 5 cm in size, suggesting the direct breakage of a relatively larger clast. This lithofacies could be generated by a storm event, during which the semi-consolidated laminated dolomitic in intertidal to supratidal was fragmented, followed by the in situ deposition and cementation by microcrystalline calcite. Alternatively, the carbonate breccia could be generated during subaerial exposure.

(LT4) Dolomitic ooid packstone/grainstone (Fig. 3i). This facies is selectively dolomitized, and the original fabric is partially preserved. Ooids remain undolomitized, but the internal structures of ooids, i.e. radial or concentric texture, are normally obliterated. The matrix is composed of coarse grained crystalline dolomite, but it is unclear whether the original interstitial spaces were filled by limy matrix or cemented by calcite spars. This lithofacies commonly deposited in a high-energy shoal environment.

(LT5) Crystalline dolostone (Fig. 9). Medium- to thick-bedded crystalline dolostones are normally composed of microcrystalline and mesocrystalline dolomite crystals. The crystal size ranges from 10 μm to 100 μm. No rock fabric or sedimentary structures can be identified.

(LT6) Bioclastic and peloidal packstone. This lithofacies commonly occurs at the bottom of shoaling upward sequence (Fig. 3e). Asymmetrical ripple marks are recognized on the upper bedding surfaces (Fig. 3c). Carbonate grains are mainly composed of bioclasts and peloids of 50 μm to 100 μm in size (Fig. 3j, k). Burrows filled with sparry calcite can be identified (Fig. 3l). This lithofacies may deposit in a shallow subtidal environment with intermittent sediment movement by waves or tidal currents.

(LT7) Lime mudstone. The lime mudstone beds are normally 1–3 m thick and occur at the bottom of a shoaling upward sequence (Fig. 3d). Absence of carbonate grains and typical sedimentary structures indicate that this lithofacies is deposited in the deep subtidal environment probably below the fair-weather wave base.

(LT8) Calcareous mudstone/shale (Fig. 3f). Calcareous mudstone/shale layers can be laterally traced in distance, representing the deep subtidal deposition.

3.2. Meter scale cycles

The Majiagou Formation is composed of a series of shoaling upward cycles (Fig. 2). Each cycle begins with deep subtidal deposition of lime mudstone or calcareous shale, followed by shallow subtidal partially dolomitized lime mudstone/wackstone, and is capped by intertidal and/or supratidal laminated dolostone. Based on the stacking pattern of lithofacies, three types of cycle can be recognized.

The type I cycle is composed of, in ascending order, thick-bedded lime mudstone, thin-bedded dolomitic lime mudstone/wackstone, crystalline dolostone, and fenestral laminated dolostone (LT7-LT2-LT5-

LT1). In most cases, not all lithofacies can be observed, and thus the type I cycle can be subdivided into four sub-types: type I-a (LT7-LT2-LT5-LT1), type I-b (LT7-LT2-LT5), type I-c (LT7-LT2-LT1) and type I-d (LT7-LT2). The absence of LT1 in type I-b cycle implies the early transgression before subaerial exposure, while there was no dolomitization in type I-d.

The type II cycle differs from the type I by the presence of calcareous shale at the base and dolomitic ooid grainstone at the top (LT8-LT7-LT5-LT4), suggesting the largest magnitude of transgression and the development of ooids shoal instead of tidal flat.

The type III cycle (LT2-LT5-LT3) clearly lacks lime mudstone at the base, indicating the smallest degree of transgression. The unique occurrence of limestone conglomerate (LT3) may represent a storm deposition, resulting in the disruption and re-deposition of laminated lime mudstone, or subaerial exposure resulting in the development of karst (Rankey, 2002).

The lower sampling interval (S1) includes 6 shoaling upward cycles (Fig. 3f). The basal cycle is about 5 m thick, and belongs to the type I-a cycle (LT7-LT2-LT5-LT1). The presence of a 30-cm thick breccia layer in the top of second cycle indicates a storm event or a prolonged subaerial exposure (the type III cycle). Absence of shallow water deposition (LT5 and LT1) in the third cycle (the type I-d) suggests the possible earliest transgression. The fourth and fifth cycles belong to the type I-b and type I-c cycles, respectively. The presence of calcareous shale at the base of the sixth cycle may suggest the largest magnitude of transgression. The cycle thickness decreases upwardly, suggesting a transgressive trend in S1.

The middle sampling interval (S2) includes 4 shoaling upward cycles, consisting of three type I-b cycle (LT7-LT2-LT5) and one type I-d cycle (LT7-LT2). This interval is characterized by the absence of intertidal-supratidal deposition of LT1, suggesting persistent submergence in seawater. All the four cycles have nearly identical thickness, implying an aggradation stacking pattern at a relatively constant sea-level.

Most part of the upper sampling interval (S3) is covered. Only two shoaling-upward cycles can be recognized. Both cycles belong to the type I-d (LT7-LT2) cycle.

4. Methods

4.1. Sample preparation

Fresh carbonate rocks were split into two parts by using a rock saw. One part was prepared to a thin section for petrographic analyses, while the mirrored polished thick sections were prepared from the other part for micro-drill sampling. Thin sections were stained with Alizarin Red-S solution to better differentiate calcite and dolomite. To avoid sampling hydrothermal veins, the sampling procedure was guided by the petrographic observation in the corresponding thin section. About 30 mg of sample powder was collected for elemental composition analysis, carbon and oxygen isotope analysis and magnesium isotope analysis by using a hand-held micro-mill. In order to capture the sub-millimetric petrographic variations, multiple powder samples were collected from the same thick section.

All carbonate samples (120, including dolostone and limestone) were subjected to petrographic and elemental composition analyses.

Table 1

Elemental and isotopic compositions of the Majiagou carbonate samples and standards.

Section	Sample No	Litho facies	Dolomite type	Fe (ppm)	Mn (ppm)	Sr (ppm)	Mn/Sr (mol/mol)	Mg/Ca (mol/mol)	$\delta^{13}\text{C}$ (‰)	$\delta^{18}\text{O}$ (‰)	$\delta^{26}\text{Mg}$ (‰)	2SD	$\delta^{25}\text{Mg}$ (‰)	2SD
S1	MJG-S1-1	LT6	Type 4	1150	83	279	0.48	0.78	-1.17	-5.89	-1.93	0.10	-0.99	0.05
	MJG-S1-18	LT5	Type 5	815	72	570	0.20	0.44	-1.43	-7.16	-2.00	0.01	-1.05	0.03
	MJG-S1-25	LT5	Type 5	1133	94	678	0.22	0.82	-1.09	-6.16	-1.92	0.07	-0.99	0.05
	MJG-S1-44	LT2	Type 2	1341	66	551	0.19	0.82	-1.44	-5.08	-1.68	0.05	-0.86	0.06
	MJG-S1-53	LT2	Type 2	1744	79	1161	0.11	0.52	-1.75	-7.91	-1.85	0.07	-0.95	0.02
	MJG-S1-57	LT2	Type 1	1142	71	921	0.12	0.86	-1.39	-5.84	-1.69	0.09	-0.87	0.05
	MJG-S1-62	LT2	Type 4	1268	74	434	0.27	0.87	-1.48	-5.05	-1.63	0.10	-0.82	0.05
	MJG-S1-63	LT1	Type 1	1387	64	553	0.18	0.86	-1.47	-5.29	-1.50	0.05	-0.79	0.02
	MJG-S1-68	LT2	Type 1	964	62	1579	0.06	0.69	-1.36	-6.07	-1.78	0.09	-0.91	0.05
	MJG-S1-69	LT4	Type 5	344	34	708	0.08	0.20	-1.70	-8.84	-1.73	0.08	-0.88	0.06
	Mean value	-	-	1129	70	743	0.19	0.69	-1.43	-6.33	-1.77	0.07	-0.91	0.04
	S2	MJG-S2-3	LT5	Type 5	795	25	481	0.08	0.86	-1.19	-6.25	-1.94	0.12	-1.00
S2	MJG-S2-4	LT5	Type 5	836	18	388	0.08	0.73	-1.51	-6.46	-1.94	0.14	-1.02	0.05
	MJG-S2-17	LT3	Type 2	1471	42	1074	0.06	0.72	-1.45	-7.34	-1.99	0.24	-1.04	0.13
	MJG-S2-19	LT2	Type 2	1086	28	676	0.07	0.85	-1.24	-5.80	-1.90	0.05	-0.99	0.03
	Mean value	-	-	1047	29	655	0.07	0.79	-1.35	-6.46	-1.94	0.14	-1.01	0.06
	S3	MJG-S3-2	LT2	Type 3	3167	178	185	1.54	0.72	-1.44	-6.82	-1.68	0.05	-0.87
S3	MJG-S3-7	LT2	Type 2	6178	414	150	4.42	0.73	-1.74	-7.76	-1.69	0.04	-0.88	0.04
	MJG-S3-10	LT6	Type 3	3227	195	40	7.87	0.93	-0.42	-6.40	-1.68	0.06	-0.87	0.01
	MJG-S3-11	LT6	Type 3	4370	263	105	4.00	0.67	-1.20	-8.19	-1.71	0.06	-0.88	0.04
	MJG-S3-12	LT1	Type 1	10,284	532	129	6.60	0.54	-2.65	-7.48	-1.75	0.10	-0.92	0.05
	Mean value	-	-	5445	316	122	4.89	0.72	-1.49	-7.33	-1.70	0.06	-0.88	0.04
	GSB-pure Mg	Std.	-	-	-	-	-	-	-	-	-2.02	0.03	-1.03	0.02
	GSB-Ca:Mg-2:1	Syn. Std.	-	-	-	-	-	-	-	-	-2.04	0.11	-1.05	0.06
GSB-Ca:Mg-4:1	GSB-Ca:Mg-4:1	Syn. Std.	-	-	-	-	-	-	-	-	-2.01	0.10	-1.03	0.06
	BHVO2	USGS. Std.	-	-	-	-	-	-	-	-	-0.20	0.02	-0.11	0.01

Notes: 2SD refers to 2 standard deviation;

GSB-Mg is an ultrapure single elemental standard solution from China Iron and Steel Research Institute.

Based on these analyses, we chose 19 dolostone samples for carbon and oxygen isotope and magnesium isotope analyses.

4.2. Petrographic analysis

Rock fabric was observed under a polarizing microscope (Nikon Eclipse LV100N POL), and crystal morphologies of dolomite were determined by field emission scanning electron microscopy (SEM, FEI Quanta 650 FEG) at Peking University. The working voltage of SEM analyses is 10 kV. The high magnification images were derived from back scattered electrons (BSE) and secondary electrons (SE).

High-magnification scanning electron microscopy-based cathodoluminescence (SEM-CL) images were obtained with a Gatan Chroma CL attached to a Quanta 650 FEG (FEI, Peking University), with a working condition of 15 kV and the working distance of 11 mm. The CL system is equipped with three detectors enable of collecting three consecutive gray-level images by sequentially using a red, green, and blue series of colour filters. Thus, a “true-colour” image that is very close to the real luminescence emitted from the sample can be constructed.

4.3. Elemental composition analysis

Approximately 10 mg of carbonate powder sample was placed in a centrifuge tube and was then dissolved by 10 mL 0.5 N acetic acid. After complete dissolution in an ultrasonic bath for 0.5 h at 50 °C, tubes with dissolved samples were centrifuged for 10 min at the speed of 3500 rpm. Supernatant was collected for the element composition determination. Major and trace element contents (Ca, Mg, Fe, Mn and Sr) were analyzed at Peking University by using a Spectro Blue Sop inductively coupled plasma optical emission spectrometer (ICP-OES) fitted with a Water Cross-flow nebulizer. All elemental concentrations were calibrated by a series of gravimetric standards with different

concentrations (ranging from 0.1 to 100 ppm) that were run before and after the measurement of every twenty samples. Standard GSR-13 was measured to assess analytical accuracy. The elemental concentrations were calculated on the basis of carbonate fraction (i.e. $\text{CaCO}_3 + \text{MgCO}_3 = 100\%$), and the analytical precision is better than 10%.

4.4. Carbon and oxygen isotope analysis

Carbonate carbon and oxygen isotopic compositions were measured by a MAT253 isotope ratio mass spectrometry (IRMS) equipped with a GasBench at Louisiana State University. About 0.2 mg of carbonate powder was reacted with 1 mL 100% phosphoric acid for 150–200 min at 72 °C to liberate CO_2 . Isotopic values are reported in δ -notation as per mil (‰) deviation relative to the Vienna-Pee Dee Formation belemnite (VPDB) standard. The analytical precision is better than 0.1‰ for $\delta^{13}\text{C}$ and 0.3‰ for $\delta^{18}\text{O}$.

4.5. Magnesium isotope analysis

The analytical procedure of Mg isotope was modified from previously published studies (Shen et al., 2013; Teng and Yang, 2014; Huang et al., 2015). Magnesium was purified by cation exchange chromatography with two columns. Remnant supernatant collected for the element composition analysis was used for Mg purification and Mg isotope analysis. A solution containing about 30 µg Mg was loaded in a Teflon beaker, and then dried down on a hot plat. The residue was redissolved in 200 µL 10 N HCl. Sample solution was eluted through column #1 (loaded with 1.8 mL Bio-Rad 200–400 mesh AG50W-X12 resin) to separate Mg from Ca. In the following column #2 (loaded with 0.5 mL Bio-Rad 200–400 mesh AG50W-X12 resin), Mg was separated from other matrix (Al, Fe, Na, and K). To ensure a clean Mg fraction, each sample was passed through column #1 twice, followed by two

passes of column #2. After column chemistry, Ca/Mg, Al/Mg, Na/Mg, K/Mg, and Fe/Mg were < 0.05, and Mg recovery rates are higher than 99%.

Magnesium isotope ratios were determined on a Nu plasma Multi-Collector Inductively Coupled Plasma Mass Spectrometer (MC-ICP-MS) at Northwest University, China. Measurements were conducted by the standard-sample bracketing method so as to correct for the instrumental mass bias and drift. Analyses were performed at low mass resolution mode, simultaneously measuring ^{26}Mg , ^{25}Mg , and ^{24}Mg . All analyses are reported in the delta notation as per mil (‰) deviation relative to the DSM-3 standard (Galy et al., 2003).

The reproducibility of Mg isotope measurements was assessed by using synthetic Mg–Ca mixed standard solution with different Mg/Ca ratios and a USGS standard BHVO-2. Multiple analyses of synthesized GSB-Mg yield $\delta^{26}\text{Mg}$ value of -2.01 to -2.04‰ (mean value: $-2.02 \pm 0.08\text{‰}$) (Table 1), which is consistent with the reported value of $-2.04 \pm 0.04\text{‰}$ (Ke et al., 2016). Results for BHVO-2 (-0.20‰) are also within the uncertainty of certified value of $-0.24 \pm 0.08\text{‰}$ (Teng, 2017).

5. Results

5.1. Petrographic classification

Based on the distribution of dolomite crystal sizes, there are unimodal and polymodal distributions, and the dolomite crystal shape can be categorized into, nonplanar, planar-s, and planar-e (cf. Sibley and Gregg, 1987). The nonplanar structure is characterized by closely packed anhedral dolomite crystals with mostly curved, lobate, serrated, or other irregular intercrystalline boundaries (Fig. 4a). The planar-e texture refers to dolomite consisting of euhedral rhombs, and the inter-crystal spaces are filled by other minerals or preserved as pores (Fig. 4b), whereas the planar-s texture is characterized by subhedral or anhedral dolomite crystals with straight crystal boundary or compromise boundaries between crystals (Fig. 4c). Furthermore, in the Folk's classification scheme (Folk, 1962), dolomite crystals can be classified into aphanocrystalline ($< 4\text{ }\mu\text{m}$), cryptocrystalline (very fine crystalline, $4\text{--}16\text{ }\mu\text{m}$), fine crystalline ($16\text{--}62\text{ }\mu\text{m}$), medium crystalline ($62\text{--}250\text{ }\mu\text{m}$), and coarse crystalline dolomite ($> 250\text{ }\mu\text{m}$). Based on the rock fabric and dolomite crystal morphology, five types of dolomite were recognized from the Majiagou samples (Table A2).

Type 1 — Aphanotopic dolomite (Fig. 5): extremely small ($< 4\text{ }\mu\text{m}$) dolomite crystals that cannot be identified by optical microscopy (Fig. 5a). The crystal morphology is best illustrated in scanning electron microscopy (SEM) (Fig. 5b-d). Under SEM, the dolomite crystals are euhedral or subhedral with straight crystal boundaries (planar-e or planar-s). The primary fenestrae structures are generally preserved by filling with finely crystalline dolomite. The type 1 dolomite is mainly

discovered in LT1 lithofacies at S1 and S3 at the top of the shoaling upward cycles, which represents the supratidal deposition.

Type 2 — Nonplanar dolomiticrite (Fig. 6): crypto-crystalline anhedral dolomite crystals ($< 16\text{ }\mu\text{m}$). The crystal morphology can only be identified under SEM, showing neighboring crystals with rounded edges and corners do not interlock significantly (Fig. 6b and c). The turbid dolomite crystals suggest the replacement of Ca-carbonate in origin (Fig. 6a). Rocks containing the type 2 dolomite are normally partially dolomitized with the preservation of some original structures (e.g. the relict algae structures, Fig. 6a). The surrounding calcitic host is dominated by sparry calcite. The type 2 dolomite occurs in LT2 and LT3 lithofacies in the type I and type III cycles at all three sampling intervals.

Type 3 — Planar dolomicroparite (Fig. 7): subhedral (planar-s) to euhedral (planar-e) fine dolomite crystals ($16\text{--}62\text{ }\mu\text{m}$). Most dolomite crystals are turbid, indicating the replacement in origin (Fig. 7a). Most dolomite crystals interlock with each other slightly (Fig. 7b and c). Rocks containing the type 3 dolomite are partially dolomitized, and are characterized by crystal-support texture with intercrystalline spaces filled by micritic calcite. In addition, the original rock fabric and texture are normally not well preserved (Fig. 7a). The type 3 dolomite occurs in LT2 and LT6 lithofacies in the type I cycles in S3.

Type 4 — Euohedral fine-crystalline dolomite (Fig. 8): dominated by euhedral rhombs of fine crystal size. Most dolomite crystals have a limpid rim and a turbid core (Fig. 8a), suggesting the replacement of an earlier carbonate phase. Inequigranular dolomite rhombs are loosely scattered in calcitic matrix (Fig. 8b and c). This kind of dolomite occurs in LT2 and LT6 lithofacies in the type I cycles in S1. Though the stratigraphic distribution of the type 4 dolomite is similar to that of the type 3 dolomite, the former (type 3) normally occurs in complete dolomitized samples.

Type 5 — Subhedral fine to medium-crystalline dolomite (Fig. 9): This type of dolomite differs from the type 4 by its subhedral and more limpid crystals, and the dolomites are tightly packed with the development of straight, compromise boundaries (Fig. 9b and c), thus the original rock fabric is normally eliminated (Fig. 9a). This kind of dolomite occurs in LT4 and LT5 lithofacies, and is discovered in the type I cycles in S1 and S2.

In summary, dolomites in the Majiagou Formation have a wide range of crystal morphologies (nonplanar, planar-s and planar-e) and crystal sizes (varying from aphanotopic to medium-crystalline). If the crystal morphology can be used to indicate generations of dolomites, the occurrences of different types of Majiagou dolomites may suggest that they might have undergone multiple generations of dolomitization process.

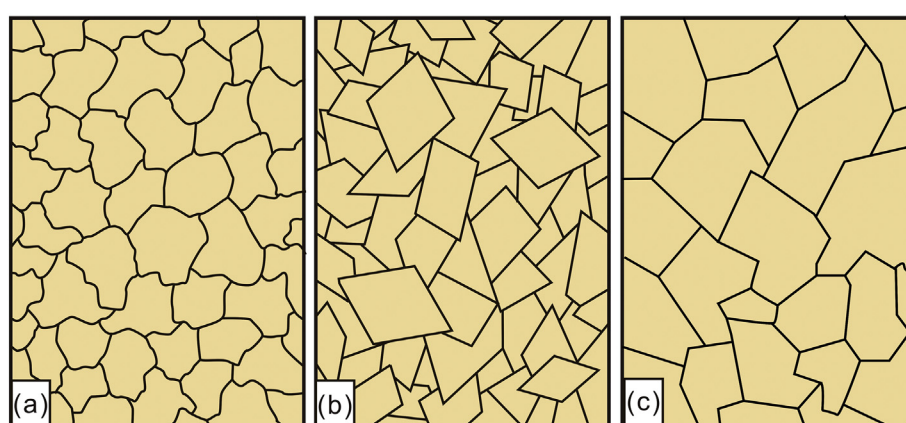


Fig. 4. Schematic diagrams of dolomite textures. (a) Nonplanar dolomite texture; (b) Planar-e dolomite texture; (c) Planar-s dolomite texture.

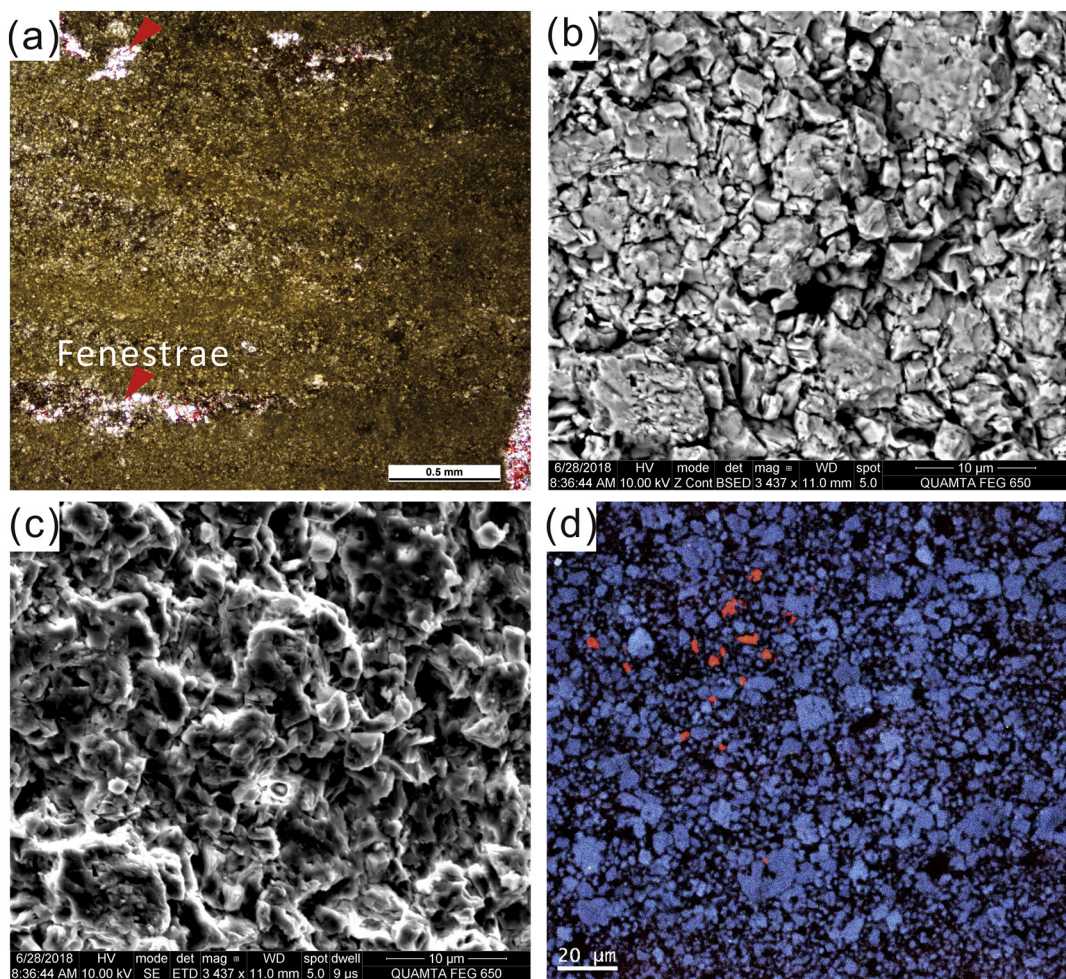


Fig. 5. Photomicrograph (a), BSED (b), SEM (c) and SEM-CL (d) images showing the crystal morphology of Type 1-aphanotopic dolomite.

5.2. Scanning electron microscopy-based cathodoluminescence

Based on the SEM-CL images, all types of dolomite display a relatively homogeneous dull luminescence and no internal zonation was observed (Fig. 5d–9d). SEM-CL image of the type 4 dolomite lack distinctive CL zones (Fig. 8d) despite having a cloudy core and clear rim in plane polarized light (Fig. 8a). In contrast, calcite cements show the similar bright orange-red luminescence in all investigated samples.

5.3. Geochemical results

The elemental compositions of all samples are plotted against depth in Fig. 2. The lower and middle sample sets have comparable Sr content, ranging from 264 to 2955 ppm (S1-mean = 920 ppm, n = 70) and from 99 to 2348 ppm (S2-mean = 602 ppm, n = 35), respectively; while the upper sample set has lower Sr content (ranging from 67 to 285 ppm, S3-mean = 167 ppm, n = 15). The upper sample set has higher Mn (S3: 21 to 612 ppm, mean = 209 ppm, n = 15) and Fe (62 to 12,439 ppm, mean = 3104 ppm, n = 15) contents, while the lower and middle sample sets have comparably lower Mn (S1: 18 to 90 ppm, mean = 47 ppm, n = 10; S2: 17 to 108 ppm, mean = 44 ppm, n = 35) and Fe (S1: 68 to 5995 ppm, mean = 820 ppm, n = 70; S2: 61 to 1286 ppm, mean = 524 ppm, n = 35) contents (Table A3). There is a clear positive correlation between Fe and Mn ($R^2 = 0.96$, $P = 2.76 \times 10^{-13}$) (Fig. 10a). In addition, S3 samples have significantly higher Mn/Sr ratios than samples from S1 and S2, while different types of dolomite in S1 and S2 have similar ranges of Fe and Mn contents, and overlapping ranges of Mn/Sr (Fig. 10a and b).

Carbonate carbon and oxygen isotopes are tabulated in Table 1, and are plotted against depth in Fig. 2. The average $\delta^{13}\text{C}$ and $\delta^{18}\text{O}$ values of the three sampling intervals are $-1.43\text{\textperthousand}$, $-1.35\text{\textperthousand}$, $-1.49\text{\textperthousand}$ and $-6.33\text{\textperthousand}$, $-6.46\text{\textperthousand}$ and $-7.33\text{\textperthousand}$, respectively. There is no correlation between $\delta^{13}\text{C}$ and $\delta^{18}\text{O}$ in all three intervals (Fig. 10c). Both $\delta^{13}\text{C}$ (type 1: -2.65 to $-1.39\text{\textperthousand}$, mean = $-1.72\text{\textperthousand}$; type 2: -1.75 to $-1.24\text{\textperthousand}$, mean = $-1.52\text{\textperthousand}$; type 3: -1.44 to $-0.42\text{\textperthousand}$, mean = $-1.02\text{\textperthousand}$; type 4: -1.48 to $-1.17\text{\textperthousand}$, mean = $-1.33\text{\textperthousand}$; type 5: -1.70 to $-1.09\text{\textperthousand}$, mean = $-1.39\text{\textperthousand}$) and $\delta^{18}\text{O}$ (type 1: -7.48 to $-5.29\text{\textperthousand}$, mean = $-6.17\text{\textperthousand}$; type 2: -7.91 to $-5.08\text{\textperthousand}$, mean = $-6.78\text{\textperthousand}$; type 3: -8.19 to $-6.40\text{\textperthousand}$, mean = $-7.14\text{\textperthousand}$; type 4: -5.89 to $-5.05\text{\textperthousand}$, mean = $-5.47\text{\textperthousand}$; type 5: -8.84 to $-6.16\text{\textperthousand}$, mean = $-6.97\text{\textperthousand}$) values of different types of dolomite have an overlapping range of variation (Fig. 10d).

Mg isotopic compositions ($\delta^{26}\text{Mg}$, ranging from $-2.0\text{\textperthousand}$ to $-1.5\text{\textperthousand}$) and Mg/Ca (molar ratios, varying between 0.20 and 0.93) of the selected 19 samples are also listed in Table 1 and plotted against depth in Fig. 2. The $\delta^{25}\text{Mg}$ vs. $\delta^{26}\text{Mg}$ cross plot is illustrated in Fig. 11a. The $\delta^{26}\text{Mg}$ values of S1 (-1.5 to $-2.0\text{\textperthousand}$, mean = $-1.77\text{\textperthousand}$) show a wider variation than S2 (-1.94 to $-1.99\text{\textperthousand}$, mean = $-1.94\text{\textperthousand}$) and S3 (-1.68 to $-1.75\text{\textperthousand}$, mean = $-1.70\text{\textperthousand}$) (Fig. 11b). The $\delta^{26}\text{Mg}$ values of different types of dolomite have an overlapping range of variation (type 1: -1.5 to $-1.78\text{\textperthousand}$, mean = $-1.68\text{\textperthousand}$; type 2: -1.68 to $-1.99\text{\textperthousand}$, mean = $-1.82\text{\textperthousand}$; type 3: -1.68 to $-1.71\text{\textperthousand}$, mean = $-1.69\text{\textperthousand}$; type 4: -1.63 to $-1.93\text{\textperthousand}$, mean = $-1.78\text{\textperthousand}$; type 5: -1.73 to $-2\text{\textperthousand}$, mean = $-1.91\text{\textperthousand}$) (Fig. 12). The Mg/Ca ratios of different types of dolomite also show similar variation (type 1: 0.54 to 0.86, mean = 0.74; type 2: 0.52 to 0.85, mean = 0.73; type 3: 0.67 to -0.93 ,

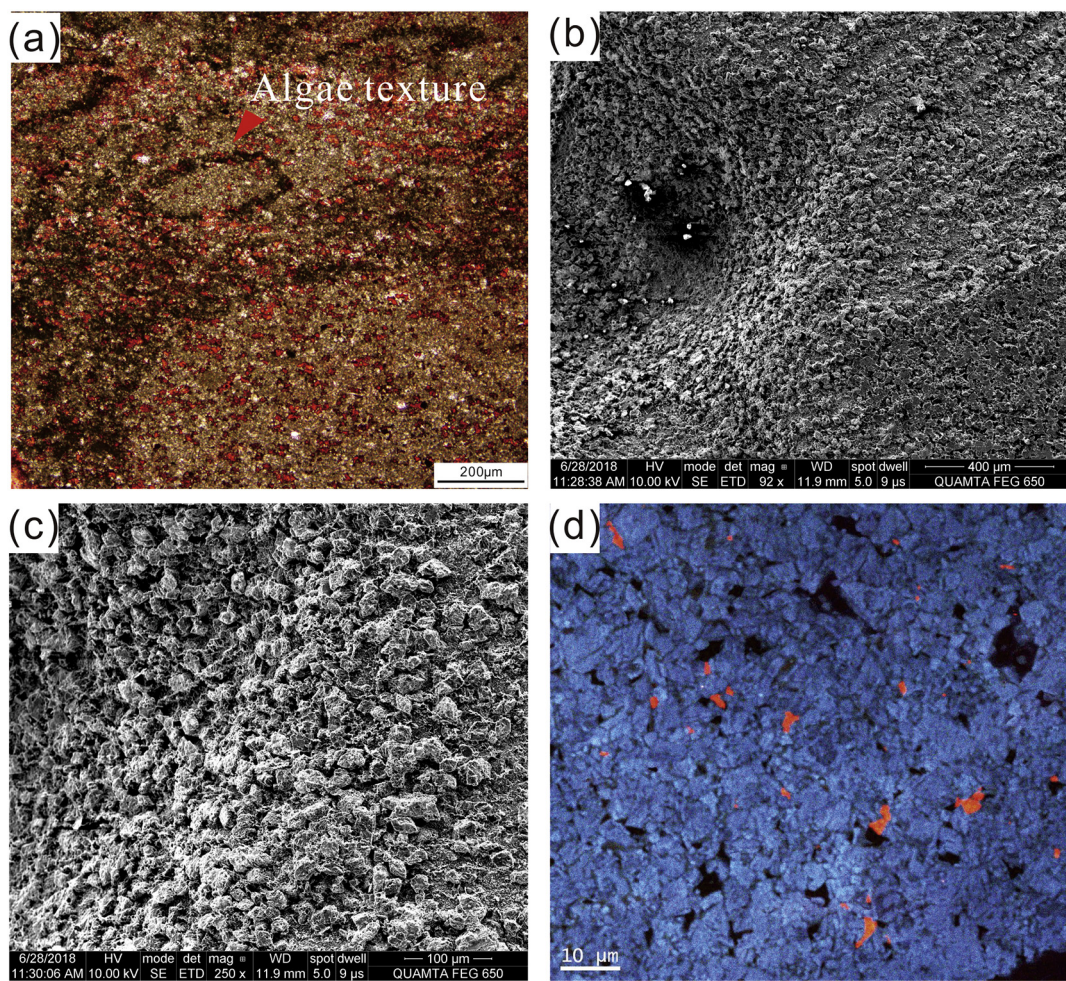


Fig. 6. Photomicrograph (a), SEM (b,c) and SEM-CL (d) images showing the crystal morphology of Type 2-nonplanar dolomiticrite.

mean = 0.78; type 4: 0.78 to 0.8, mean = 0.83; type 5: 0.2 to 0.86, mean = 0.61).

6. Interpretation and discussion

6.1. Geochemical composition of the Majiagou dolomite

Carbonate carbon and oxygen isotopes and trace element (Fe, Mn, Sr) compositions can be influenced by many factors, and may provide valuable information about the diagenetic history of carbonate rocks (Arosi and Wilson, 2015; Siahi et al., 2018). For example, with an increasing degree of meteoric diagenesis, carbonate rocks tends to lose Sr and gain Fe and Mn, resulting in an increase of Mn/Sr ratio (Jacobsen and Kaufman, 1999; Halverson et al., 2007; Webb et al., 2009; Siahi et al., 2018). In addition, carbonate $\delta^{18}\text{O}$ decreases with an intensified water-rock interaction (Knauth and Kennedy, 2009). Furthermore, if organic matter degradation is also involved in diagenesis, a positive correlation between $\delta^{13}\text{C}$ and $\delta^{18}\text{O}$ is often apparent (Fairchild et al., 1990; Xiao et al., 1997). Although it is unclear how the aforementioned geochemical proxies could be modified during dolomitization processes, it is reasonable to speculate that dolomites derived from different dolomitization processes might have various geochemical compositions (Land, 1980; Warren, 2000).

Different types of dolomites from the Majiagou Formation have similar trace element composition and overlapping ranges of $\delta^{13}\text{C}$ and $\delta^{18}\text{O}$ values (Fig. 10). Similar conclusions can be drawn from the SEM-CL imaging. All types of dolomite show a relatively dull luminescence (indicating either low Mn and Fe, or just generally low Mn) (Machel,

1985). And the absence of zonation within dolomite crystals (Fig. 5d–9d) implies invariant porewater geochemical composition during the growth of dolomite crystals (Hiatt and Pufahl, 2014). In contrast, calcite cements show bright orange-red luminescence, suggesting an elevated Mn content but relatively low Fe concentration. These observations indicate that the generation of the five types of dolomites in the Majiagou Formation cannot readily be differentiated by either cathodoluminescence imaging or the traditional geochemical proxies.

6.2. Mg isotope systematics of dolomite in the Majiagou Formation

Carbonate samples (including dolostone and dolomitic limestone) from S1 show a negative linear correlation between $\delta^{26}\text{Mg}$ and $1/\text{[Mg]}$ (given the uncertainties of $\delta^{26}\text{Mg}$, $R^2 = 0.82$; $P = 7.35 \times 10^{-4}$) (Fig. 12), suggesting that these specimens can be defined by a binary mixing between the calcite and dolomite components with fixed Mg isotopic composition (Li et al., 2016; Peng et al., 2016). It should be noted that one sample (MJG-S1–69) was excluded from the calculation of relationship between $\delta^{26}\text{Mg}$ and $1/\text{[Mg]}$ due to dedolomitization, which lowers Mg/Ca ratio but retains $\delta^{26}\text{Mg}$ (Jacobson et al., 2010; Perez-Fernandez et al., 2017).

In addition, dolomite samples with different crystal morphology from S2 and S3 have nearly identical $\delta^{26}\text{Mg}$ (Fig. 12). Thus, different types of dolomite from the same sampling interval have nearly identical $\delta^{26}\text{Mg}$ values, regardless of the crystal morphology and overall rock fabric. Similar observations have been reported from dolostone of other ages. For example, three types of dolomite (dolomicrite, subhedral dolomite and anhedral dolomite) from the Mesoproterozoic Wumishan

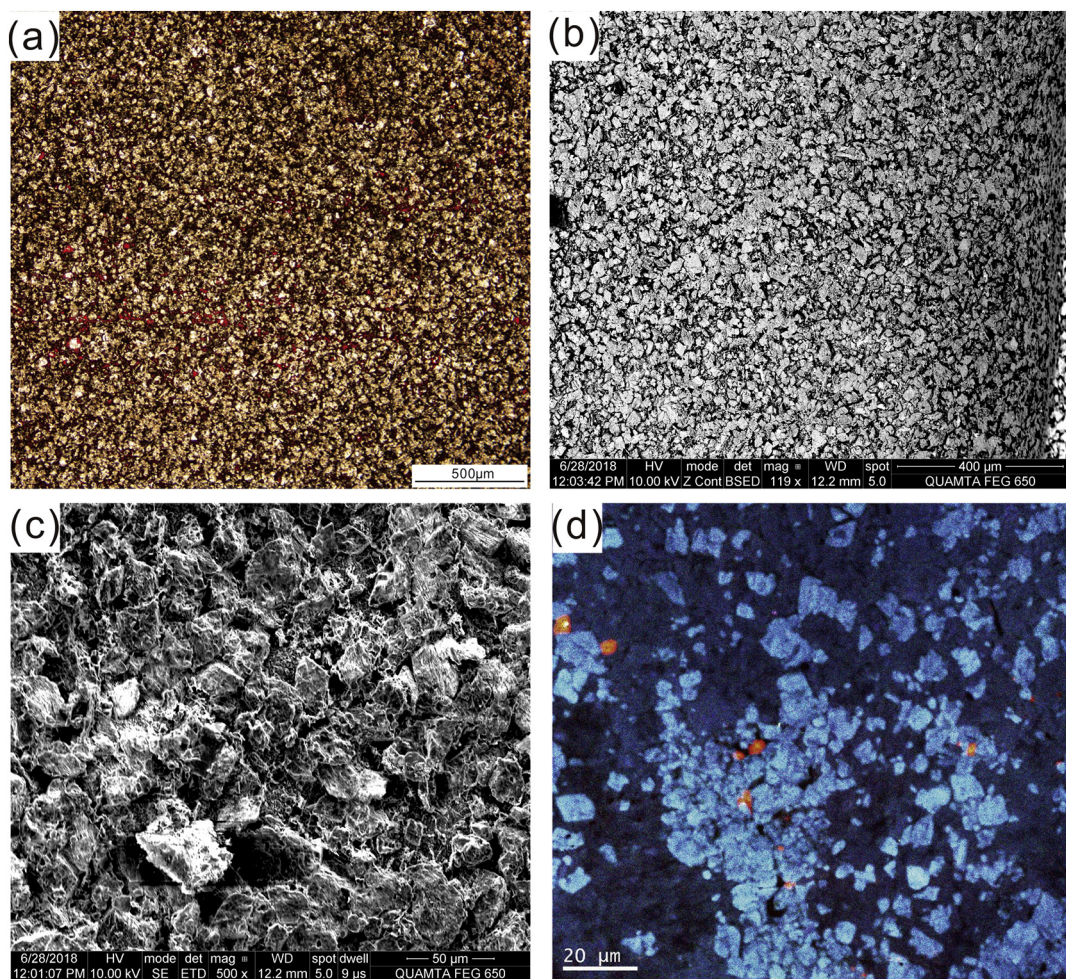


Fig. 7. Photomicrograph (a), BSED (b), SEM (c) and SEM-CL (d) images showing the crystal morphology of Type 3-planar dolomicrosparite, (b) and (c) show the subhedral to euhedral fine dolomite crystals.

Formation have similar $\delta^{26}\text{Mg}$ values, ranging from $-1.35\text{\textperthousand}$ to $-1.72\text{\textperthousand}$, suggesting that there is no clear relationship between $\delta^{26}\text{Mg}$ and dolomite crystal morphology and rock fabric (Huang et al., 2015).

In fact, the Mg isotopic composition of dolomite is determined by both the Mg isotopic composition of dolomitization fluids and the processes of dolomitization. There are two types of dolomitization processes: dolomitization by advective flow and seawater dolomitization. In the advective flow dolomitization process, dolomitization fluids percolate through the calcareous sediments via advective flow and result in the dolomitization of precursor Ca-carbonate, which can be simulated by the AF model (Peng et al., 2016). In most traditional dolomitization models such as the brine-reflux model (Adams and Rhodes, 1960; Aharon et al., 1977), the marine-meteoric mixing model (Hanshaw et al., 1971) and the hydrothermal model (Davies and Smith, 2006), advection is the major process of Mg transfer. Based on the AF model, Mg isotopic composition of dolomite is determined by five factors, including the isotopic composition of dolomitization fluid, isotopic fractionation during dolomitization, temperature, sedimentation rate, and reaction rate of dolomitization (Huang et al., 2015). Among the five parameters, isotopic fractionation at low temperature has been determined with relatively small uncertainty (ranging from 1.8 to 2.1‰ between 0 °C and 25 °C) (Immenhauser et al., 2010; Mavromatis et al., 2013; Fantle and Higgins, 2014; Blättler et al., 2015; Li et al., 2015; Wang et al., 2017), while the isotopic composition of dolomitization fluid is determined by the source of Mg. The in situ, i.e. in the locality of dolomite formation, isotopic composition of dolomitization fluid is also a function of distance from the source and the velocity of fluid flow

(Peng et al., 2016).

On the other hand, seawater dolomitization refers to the dolomitization process (such as the Sabkha model) without significant advection of fluids, and Mg being supplied by diffusion (Shinn, 1965). This dolomitization process can be simulated by the DAR model (Huang et al., 2015; Peng et al., 2016). In the DAR process, Mg isotopic composition of dolomite is determined by the seawater Mg isotopic composition, isotopic fractionation during dolomitization, temperature, sedimentation rate, and reaction rate of dolomitization (Huang et al., 2015). Although there are hints that the $\delta^{26}\text{Mg}$ of seawater could change relatively quickly (Pogge von Strandmann et al., 2014), $\delta^{26}\text{Mg}$ of seawater may not change significantly within relative short time interval (< 1 million years) (Blättler et al., 2015), although temperature alone could affect both the coefficient of diffusivity of Mg as well as the fractionation factor for dolomitization (Li et al., 2015; Hu et al., 2017). In addition, sedimentary rate varies depending on the depositional environments. Therefore, variation of sedimentation rate of different lithofacies may also cause variation of $\delta^{26}\text{Mg}$ of dolostone (Huang et al., 2015).

Thus, in either dolomitization model (DAR or AF), the Mg isotopic composition of dolomite is affected by a number of factors. Dolomite with similar $\delta^{26}\text{Mg}$ is most parsimoniously interpreted as having the same origin, i.e. having precipitated in the same dolomitization event. It is unlikely that dolomite generated from two different processes, e.g. seawater dolomitization and reflux dolomitization, could have the same $\delta^{26}\text{Mg}$, even with the same Mg source, e.g. seawater. Therefore, similar $\delta^{26}\text{Mg}$ values shared by different types of dolomite within the same

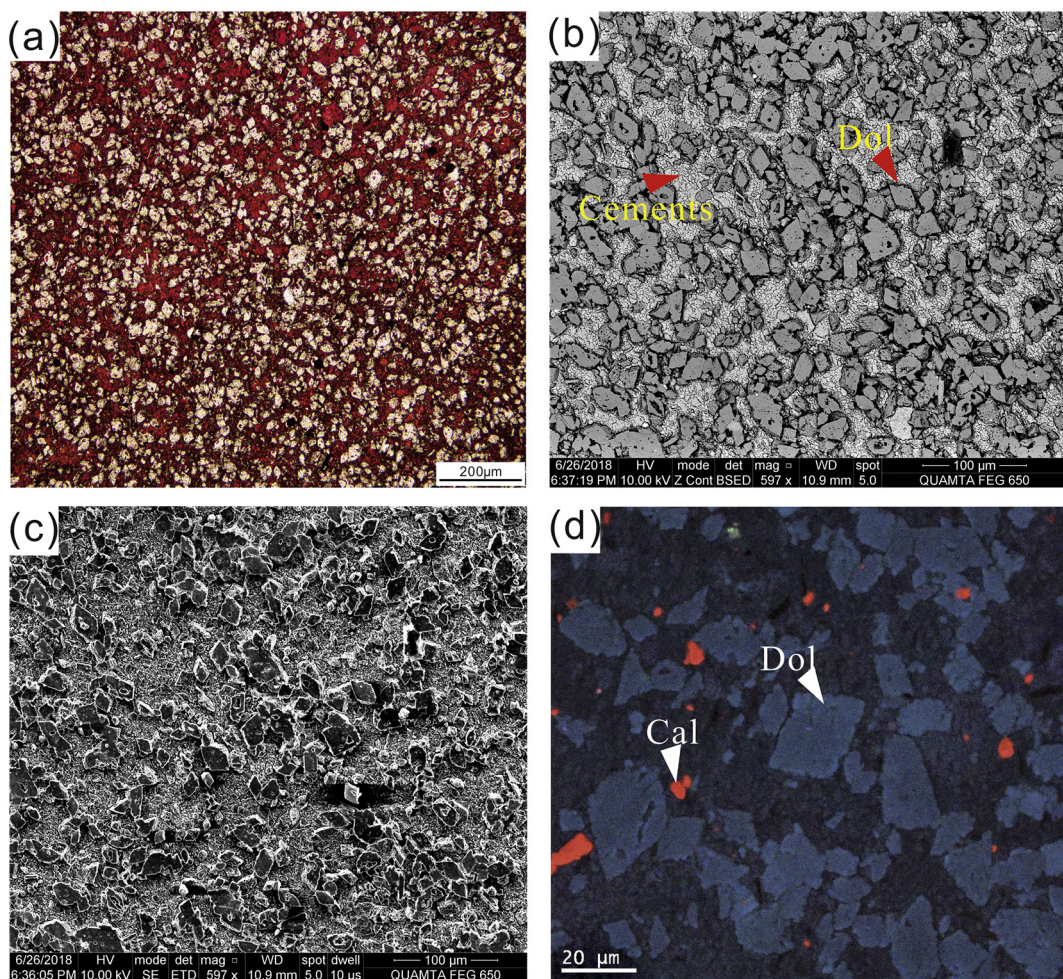


Fig. 8. Photomicrograph (a), BSED (b), SEM (c) and SEM-CL (d) images showing the crystal morphology of Type 4-euhedral fine crystalline dolomite, (b) and (c) images show the euhedral crystals (Dol) held in matrix of micritic calcite (Cal).

sampling interval may suggest that these dolomites may derive from a single dolomitization process.

6.3. Interpretation of the dolomite crystal morphology

6.3.1. Why crystal morphology was used to distinguish different generations of dolomites

It has been proposed that dolomites with the same fabric and crystal morphology were subjected to similar rates of nucleation and growth (Sibley and Gregg, 1987; Gregg et al., 2015), while both the nucleation and growth rates are temperature-dependent and are related to the level of saturation of dolomitization fluids. Below the ‘critical roughening temperature’ (CRT) and with low degree of supersaturation, crystal growth occurs by nucleation at active sites and lateral migration of layers or growth spirals, forming faceted crystals and planar interfaces. In contrast, above CRT or at a high degree of supersaturation, crystal growth occurs by random addition of atoms to the crystal surface, resulting in the nonplanar dolomite crystals (Sibley and Gregg, 1987). It was suggested that the CRT for dolomite was between 50 and 1000 °C. Thus, the non-planar (xenotopic) fabric should result from the burial dolomitization of precursor limestone or recrystallization of earlier-formed near-surface dolomite at depth, whereas dolomite with planar crystals may precipitate at lower temperatures (Gregg and Sibley, 1984).

On the other hand, the crystal size is then determined by the rate difference between nucleation and crystal growth (Genck, 1969). A high density of nucleation sites in a substrate and/or a high degree of

supersaturation favor the precipitation of finely crystalline dolomites, while coarser dolomite crystals would be precipitated when the growth rate exceeds the nucleation rate (Sibley and Gregg, 1987). Generally, rocks consisting of fine-grained Ca-carbonate precursors offer more potential nucleation sites, and thus tend to be replaced by fine crystalline dolomite and favor the retention of original rock fabric (Bullen and Sibley, 1984; Sibley, 1991). In contrast, coarser-grained Ca-carbonate that contains fewer nucleation sites are likely replaced by large dolomite crystals, resulting in the obliteration of original textures. Thus, the early-formed dolomite crystals tend to be smaller than the late diagenetic or burial dolomites (Sachan, 1993). This may explain very fine grained dolomite (0.5–5 µm) formed early in modern evaporitic setting (McKenzie, 1981). In addition, dolomites with the unimodal size distribution may indicate a single phase of dolomitization (Sibley et al., 1993).

For above reasons, dolomite crystal morphology has been widely used to differentiate dolomite formed at low temperature near surface from high temperature dolomite formed during deep burial or hydrothermal processes (Amthor and Friedman, 1991; Sachan, 1993; Zheng et al., 1994).

Therefore, based on the crystal morphology and rock fabric alone, the Majiagou carbonate might have undergone at least three generations of dolomitization. The earliest stage of dolomitization might have occurred near the surface, and is represented by the Type 1 dolomite, which has extremely fine crystal size and euhedral or subhedral crystal morphology (Fig. 5). The type 3 and type 4 dolomite may derive from dolomitization at higher temperature in deeper depth. The Type 2

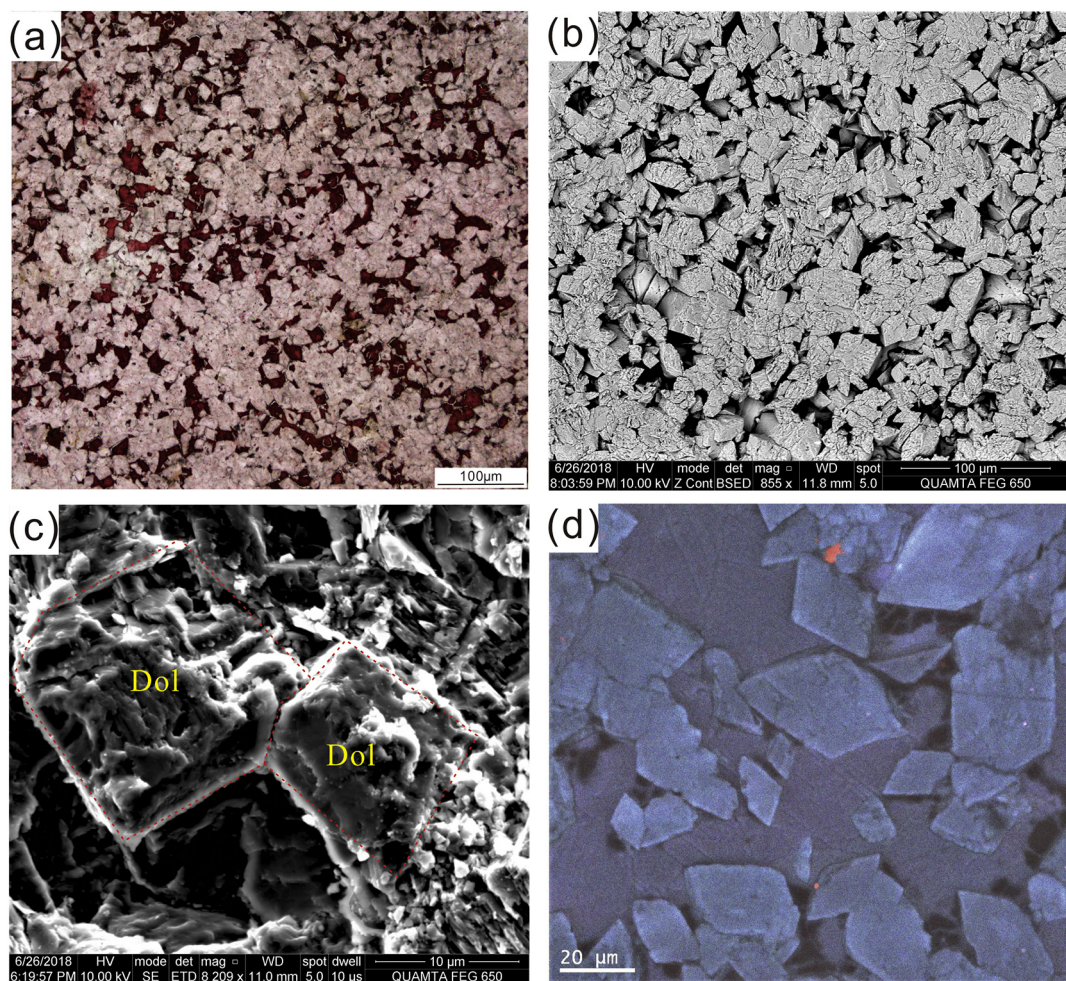


Fig. 9. Photomicrograph (a), BSED (b), SEM (c) and SEM-CL (d) images showing the crystal morphology of Type 5-subhedral fine to medium crystalline dolomite. Crystals are subhedral to anhedral with straight, compromise boundaries and crystal-face junctions (b, c).

dolomite that is characterized by non-planar crystal boundary may indicate dolomitization above CRT in deep burial. The Type 5 dolomite with coarser crystals that eliminate the original rock fabric may indicate recrystallization. It is highly likely that both the Type 2 and Type 5 dolomite may form at high temperatures in deep burial.

6.3.2. Why crystal morphology cannot be used to distinguish different generations of dolomites

Our study, however, reveals that dolomites of different crystal morphology and crystal size have identical $\delta^{26}\text{Mg}$, suggesting that different types of dolomite might have originated from the same phase of dolomitization. This finding seems to contradict with the argument that dolomite crystal morphology and crystal size can be used to differentiate the generation of dolomitization processes. Such discrepancy can be interpreted in two ways. In the first scenario, the crystal morphology may not be controlled by temperature alone, and additional factors need to be considered as well. For example, incorporation of magnesium may modify the calcite crystal morphology, resulting in the formation of rounded rhombohedral calcite crystals (Davis et al., 2000; Davis et al., 2004; Zhang et al., 2013; Hong et al., 2016). Dolomite crystal morphology could be affected by the mineralogy of precursor Ca-carbonate, i.e., aragonite, high-Mg calcite, or low-Mg calcite. It has been noted that high-Mg calcite and aragonite are preferentially dolomitized, and the fabric retention dolomitization is favored in high-Mg calcite precursors (Bullen and Sibley, 1984). Thus, it is reasonable to speculate that the lithology of host rock might have played an important role in controlling the dolomite crystal morphology and the

retention of rock fabric.

Alternatively, the crystal morphology might be modified during diagenesis or deep burial processes. For example, some non-planar dolomite crystals are considered to reflect the competition for growth space during crystal overgrowths (Jones, 2005), but the Mg isotopic composition could be preserved in these processes due to the conservative nature of dolomite Mg isotopes (Geske et al., 2012; Azmy et al., 2013; Hu et al., 2017). It is plausible that the early-formed fine grained dolomites are usually non-stoichiometric, poorly ordered, and thus more reactive. Recrystallization during deep burial could generate coarser grained dolomite with non-planar crystal boundaries when temperatures approach the CRT (Gregg and Sibley, 1984). In contrast, coarser-grained dolomite, such as those formed in the mixing-zone and seepage-reflux dolomitization, may be resistant to recrystallization since their compositions are more stoichiometric and the crystal lattices are better ordered. On the other hand, the coarser-grained dolomite may also convert to xenotopic crystal when temperatures exceed the CRT (Tucker and Wright, 2009). Therefore, some high temperature feature, such as the non-planar crystal edges and coarse crystals, might derive from neomorphism of planar aphanotopic or microcrystalline dolomite formed at shallower depth (Winkelstern and Lohmann, 2016).

In either case, our study indicates that dolomite crystal morphology and rock fabric alone may not provide the unique constraint on the generations of dolomitization. Interpretation of dolomite generation should combine petrographic observations, traditional geochemical proxies, and some novel unconventional isotopes, such as Mg isotopes.

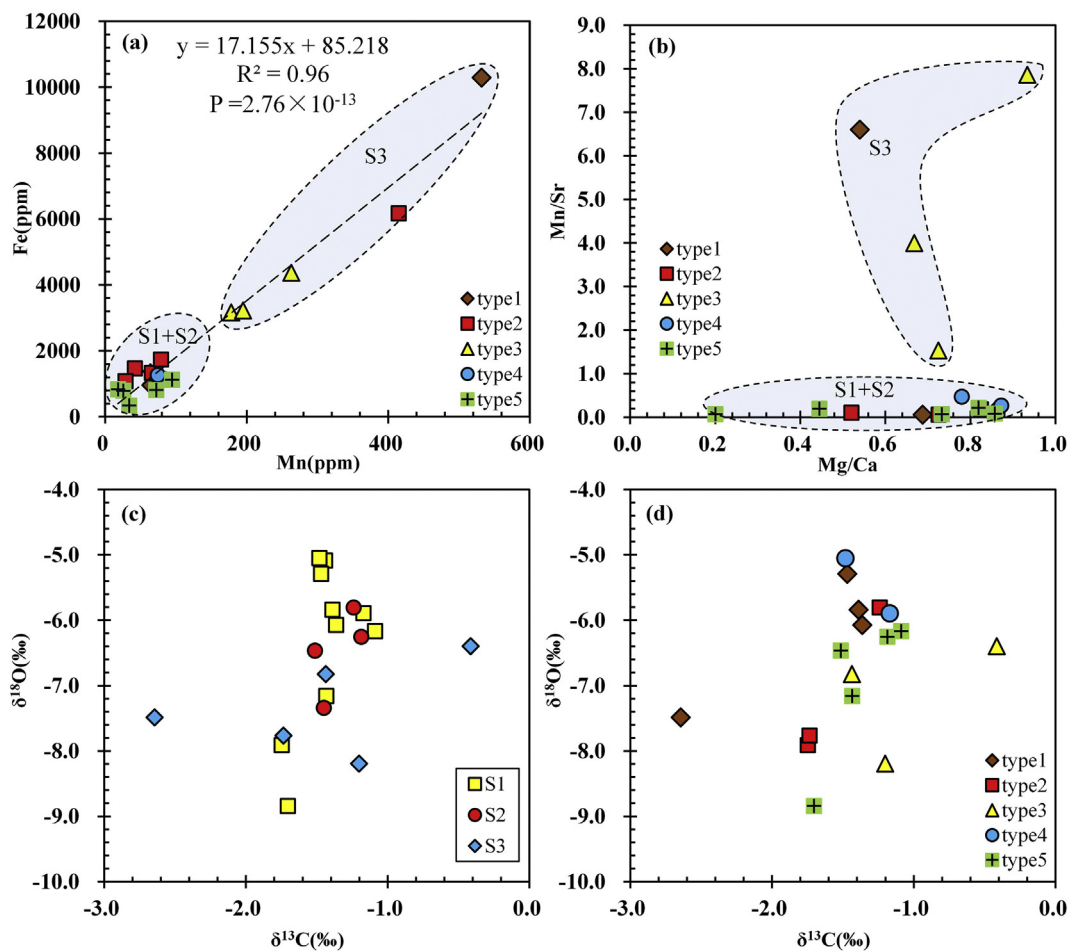


Fig. 10. Crossplots of element compositions, $\delta^{13}\text{C}$ and $\delta^{18}\text{O}$ data of the Majiagou carbonate samples (a) Fe_{carb} vs. Mn_{carb} , showing a positive correlation in S3. (b) Mg/Ca (molar ratio) vs. Mn/Sr (molar ratio). (c) $\delta^{13}\text{C}$ vs. $\delta^{18}\text{O}$ for dolomites from different sections. (d) $\delta^{13}\text{C}$ vs. $\delta^{18}\text{O}$ from different types of dolomite.

7. Conclusions

Five types of dolomite with distinct crystal morphology and rock fabric were identified from the middle Ordovician Majiagou Formation in North China. Different types of dolomite have overlapping ranges of elemental compositions (Mn, Fe, Sr) and isotopic compositions of carbon and oxygen isotopes. There is a negative linear correlation

between $\delta^{26}\text{Mg}$ and $1/\text{[Mg]}$ for partially dolomitized limestone samples in S1, indicating a binary mixing between the calcite and dolomite components with fixed isotopic composition, while the dolostone samples from S2 and S3 have nearly identical $\delta^{26}\text{Mg}$, respectively. These observations suggest that different types of dolomites in the same sampling interval might have the same $\delta^{26}\text{Mg}$ values. Because $\delta^{26}\text{Mg}$ of dolostone is not only controlled by the composition of dolomitization

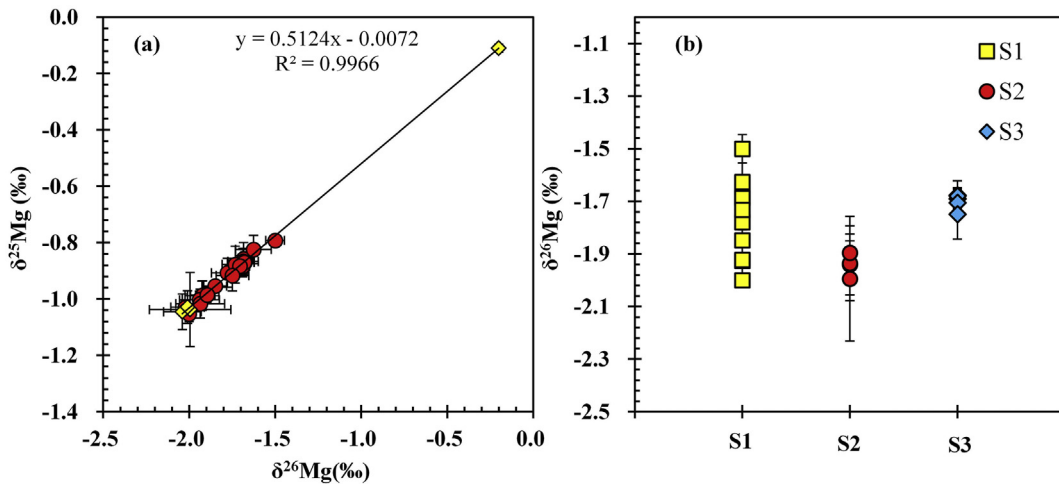


Fig. 11. (a) $\delta^{26}\text{Mg}$ vs. $\delta^{25}\text{Mg}$ crossplot for the carbonate samples from the Majiagou Formation (red marks) and standards (yellow marks). (b) $\delta^{26}\text{Mg}$ of carbonate from different sampling intervals. (For interpretation of the references to colour in this figure legend, the reader is referred to the web version of this article.)

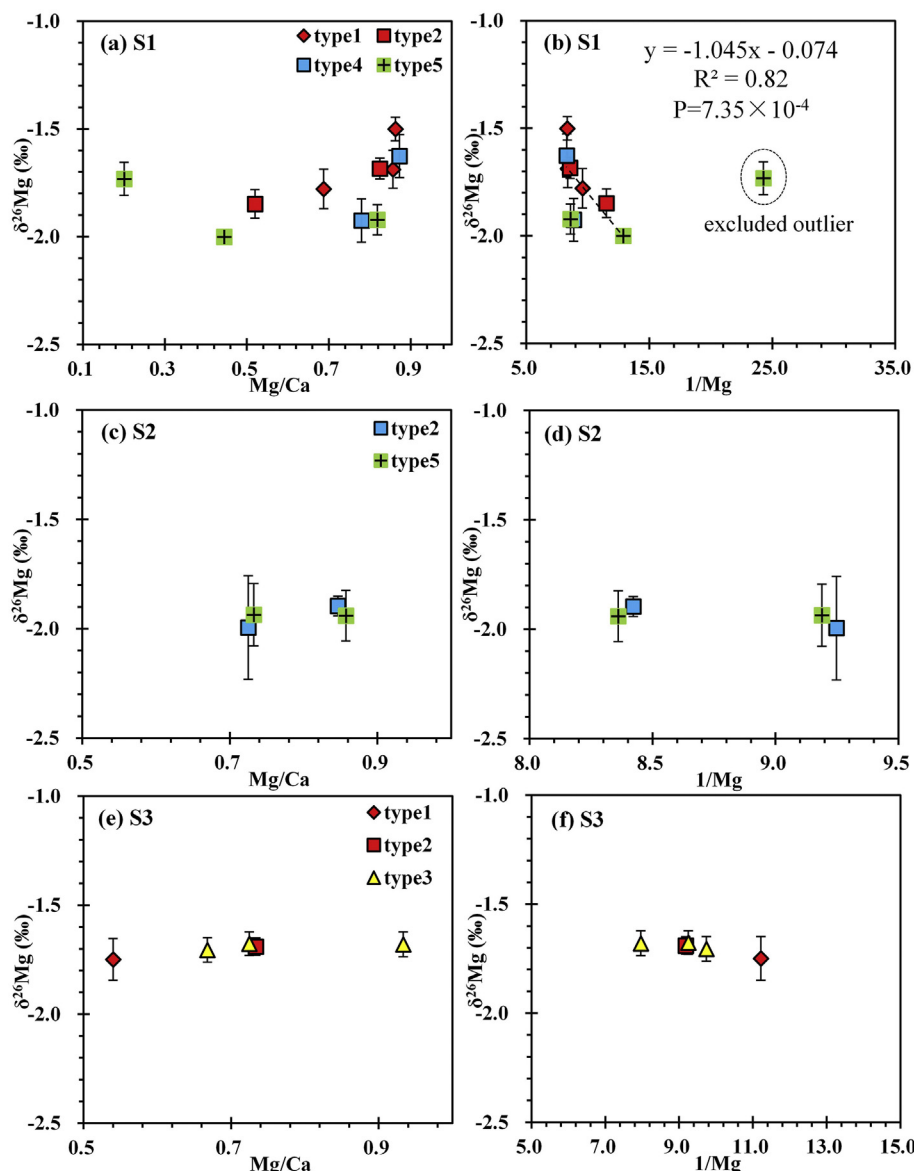


Fig. 12. Crossplots of Mg/Ca vs. $\delta^{26}\text{Mg}$, and $1/\text{[Mg]}$ vs. $\delta^{26}\text{Mg}$. There is a negative linear correlation between $1/\text{[Mg]}$ and $\delta^{26}\text{Mg}$ in S1, suggesting a binary mixing between the calcite and dolomite components.

fluids, but also by the process of dolomitization, dolomites with similar $\delta^{26}\text{Mg}$ values are most parsimoniously interpreted as origination in a same stage of dolomitization. Therefore, different types of dolomite with distinct crystal morphology and rock fabric may derive from the same dolomitization process. There are two possible interpretations to the contradictory conclusions drawn from the dolomite morphology and Mg isotopes: (a) The dolomite crystal morphology may not be controlled by the formation temperature alone, or (b) the crystal morphology might derive from recrystallization of earlier formed dolomite in deep burial, while the Mg isotope system is still preserved. In either case, our study suggests that dolomite crystal morphology alone may not necessarily indicate the generations of dolomite.

Acknowledgments

We thank Jieqiong Chang, Yixin Cui and Zhe Wang for field assistance. We also thank Zhouqiao Zhao for laboratory assistance. This work was supported by the National Natural Science Foundation of China [grant numbers 41772359, 41602343]. We thank two anonymous reviewers and editor for their constructive comments and

suggestions for improving the manuscript.

Appendices. Supplementary data

Supplementary data to this article can be found online at <https://doi.org/10.1016/j.chemgeo.2019.04.007>.

References

- Adams, J.E., Rhodes, M.L., 1960. Dolomitization by seepage refluxion. AAPG Bull. 44, 1912–1920. <https://doi.org/10.1306/0BDA263-16BD-11D7-8645000102C1865D>.
- Aharon, P., Kolodny, Y., Sass, E., 1977. Recent hot brine dolomitization in the “Solar Lake,” Gulf of Elat: isotopic, chemical, and mineralogical study. J. Geol. 85, 27–48. <https://www.jstor.org/stable/30068675>.
- Allan, J.R., Wiggins, W.D., 1993. Dolomite Reservoirs: Geochemical Techniques for Evaluating Origin and Distribution. AAPG Continuing Education Course Notes Series, vol. 36. American Association of Petroleum Geologists, Tulsa, OK, pp. 262–263.
- Amthor, J.E., Friedman, G.M., 1991. Dolomite-rock textures and secondary porosity development in Ellenburger Group carbonates (Lower Ordovician), west Texas and southeastern New Mexico. Sedimentology 38, 343–362. <https://doi.org/10.1111/j.1365-3091.1991.tb01264.x>.
- Arosi, H.A., Wilson, M.E.J., 2015. Diagenesis and fracturing of a large-scale, syntectonic carbonate platform. Sediment. Geol. 326, 109–134. <https://doi.org/10.1016/j.sedgeo.2015.06.003>.

- sedgeo.2015.06.010.
- Arvidson, R.S., Mackenzie, F.T., 1999. The dolomite problem: control of precipitation kinetics by temperature and saturation state. *Am. J. Sci.* 299, 257–288. <https://doi.org/10.2475/ajs.299.4.257>.
- Azmy, K., Lavoie, D., Knight, I., Chi, G., 2008. Dolomitization of the Lower Ordovician Aguathuna Formation carbonates, Port au Port Peninsula, western Newfoundland, Canada: implications for a hydrocarbon reservoir. *Can. J. Earth Sci.* 45, 795–813. <https://doi.org/10.1139/E08-020>.
- Azmy, K., et al., 2013. Magnesium-isotope and REE compositions of Lower Ordovician carbonates from eastern Laurentia: Implications for the origin of dolomites and limestones. *Chem. Geol.* 356, 64–75. <https://doi.org/10.1016/j.chemgeo.2013.07.015>.
- Blättler, C.L., Miller, N.R., Higgins, J.A., 2015. Mg and Ca isotope signatures of authigenic dolomite in siliceous deep-sea sediments. *Earth Planet. Sci. Lett.* 419, 32–42. <https://doi.org/10.1016/j.epsl.2015.03.006>.
- Braithwaite, C.J.R., Rizzi, G., Darke, G., 2004. *The Geometry and Petrogenesis of Dolomite Hydrocarbon Reservoirs*. Geological London, London, UK.
- Buhl, D., Immenhauser, A., Smeulders, G., Kabiri, L., Richter, D.K., 2007. Time series $\delta^{26}\text{Mg}$ analysis in speleothem calcite: kinetic versus equilibrium fractionation, comparison with other proxies and implications for palaeoclimate research. *Chem. Geol.* 244, 715–729. <https://doi.org/10.1016/j.chemgeo.2007.07.019>.
- Bullen, S.B., Sibley, D.F., 1984. Dolomite selectivity and mimic replacement. *Geology* 12, 655–658. [https://doi.org/10.1130/0091-7613\(1984\)12-655-658](https://doi.org/10.1130/0091-7613(1984)12-655-658).
- Carder, E.A., Galy, A., McKenzie, J.A., Vasconcelos, C., Elderfield, H., 2005a. Magnesium Isotopic Evidence for Widespread Microbial Dolomite Precipitation in the Geological Record. In: AGU Fall Meeting Abstracts, abstract id. V41F-1527.
- Carder, E.A., Galy, A., McKenzie, J.A., Vasconcelos, C., Elderfield, H.E., 2005b. Magnesium isotopes in bacterial dolomites: a novel approach to the dolomite problem. *Geochim. Cosmochim. Acta* 69, A213.
- Chang, V.T., Williams, R.J., Makishima, A., Belshaw, N.S., O'Nions, R.K., 2004. Mg and Ca isotope fractionation during CaCO_3 biomineralisation. *Biochem. Biophys. Res. Commun.* 323, 79–85. <https://doi.org/10.1016/j.bbrc.2004.08.053>.
- Chen, X., et al., 2015. Sedimentary facies and palaeogeography of the North China region during the Ordovician. *Sediment. Geol. Tethyan Geol.* 1–11.
- Conliffe, J., Azmy, K., Greene, M., 2012. Dolomitization of the lower Ordovician Catoche formation: Implications for hydrocarbon exploration in western Newfoundland. *Mar. Pet. Geol.* 30, 161–173. <https://doi.org/10.1016/j.marpetgeo.2011.10.007>.
- Daughtry, A.C., Perry, D., Williams, M., 1962. Magnesium isotopic distribution in dolomite. *Geochim. Cosmochim. Acta* 26, 857–866.
- Davies, G.R., Smith, L.B., 2006. Structurally controlled hydrothermal dolomite reservoir facies: an overview. *AAPG Bull.* 90, 1641–1690. <https://doi.org/10.1306/05220605164>.
- Davis, R.A., Dalrymple, R.W., 2012. *Principles of Tidal Sedimentology*. Springer Netherlands, Dordrecht.
- Davis, K.J., Dove, P.M., De Yoreo, J.J., 2000. The Role of Mg^{2+} as an impurity in calcite growth. *Science* 290, 1134–1137. <https://doi.org/10.1126/science.290.5494.1134>.
- Davis, K.J., Dove, P.M., Wasylenki, L.E., De Yoreo, J.J., 2004. Morphological consequences of differential Mg^{2+} incorporation at structurally distinct steps on calcite. *Am. Mineral.* 89, 714–720. <https://doi.org/10.2138/am-2004-5-605>.
- Fairbridge, R.W., 1957. The dolomite question. In: LeBlanc, R.J., Breeding, J.G. (Eds.), *Regional Aspects of Carbonate Deposition*. SEPM Society for Sedimentary Geology, Tulsa, OK, pp. 125–178.
- Fairchild, I., Marshall, J., Bertrand-Sarfati, J., 1990. Stratigraphic shifts in carbon isotopes from Proterozoic stromatolitic carbonates (Mauritania): influences of primary mineralogy and diagenesis. *Am. J. Sci.* 290, 46–79.
- Fantle, M.S., Higgins, J.A., 2014. The effects of diagenesis and dolomitization on Ca and Mg isotopes in marine platform carbonates: Implications for the geochemical cycles of Ca and Mg. *Geochim. Cosmochim. Acta* 142, 458–481. <https://doi.org/10.1016/j.gca.2014.07.025>.
- Folk, R.L., 1962. Spectral Subdivision of Limestone Types1. In: Ham, W.E. (Ed.), *Classification of Carbonate Rocks—A Symposium*. American Association of Petroleum Geologists, Tulsa, OK, pp. 62–84.
- Galy, A., Bar-Matthews, M., Halicz, L., O'Nions, R.K., 2002. Mg isotopic composition of carbonate: insight from speleothem formation. *Earth Planet. Sci. Lett.* 201, 105–115. [https://doi.org/10.1016/S0012-821X\(02\)00675-1](https://doi.org/10.1016/S0012-821X(02)00675-1).
- Galy, A., et al., 2003. Magnesium isotope heterogeneity of the isotopic standard SRM980 and new reference materials for magnesium-isotope-ratio measurements. *J. Anal. At. Spectrom.* 18, 1352–1356. <https://doi.org/10.1039/B309273A>.
- Genck, W.J., 1969. Temperature Effects of Growth and Nucleation Rates in Mixed Suspension Crystallization. Iowa State University, Ames, IA.
- Geske, A., et al., 2012. Impact of diagenesis and low grade metamorphism on isotope ($\delta^{26}\text{Mg}$, $\delta^{13}\text{C}$, $\delta^{18}\text{O}$ and $\delta^{87}\text{Sr}$ - $\delta^{86}\text{Sr}$) and elemental (Ca, Mg, Mn, Fe and Sr) signatures of Triassic sabkha dolomites. *Chem. Geol.* 332–333, 45–64. <https://doi.org/10.1016/j.chemgeo.2012.09.014>.
- Geske, A., et al., 2015a. The magnesium isotope ($\delta^{26}\text{Mg}$) signature of dolomites. *Geochim. Cosmochim. Acta* 149, 131–151. <https://doi.org/10.1016/j.gca.2014.11.003>.
- Geske, A., et al., 2015b. Magnesium isotope composition of sabkha porewater and related (Sub-)recent stoichiometric dolomites, Abu Dhabi (UAE). *Chem. Geol.* 393–394, 112–124. <https://doi.org/10.1016/j.chemgeo.2014.11.020>.
- Gregg, J.M., Sibley, D.F., 1984. Epigenetic dolomitization and the origin of xenotopic dolomite texture. *J. Sediment. Res.* 54, 908–931. <https://doi.org/10.1306/212F8535-2B24-11D7-8648000102C1865D>.
- Gregg, J.M., Bish, D.L., Kaczmarek, S.E., Machel, H.G., 2015. Mineralogy, nucleation and growth of dolomite in the laboratory and sedimentary environment: a review. *Sedimentology* 62, 1749–1769. <https://doi.org/10.1111/sed.12202>.
- Halverson, G.P., Dudás, F.Ó., Maloof, A.C., Bowring, S.A., 2007. Evolution of the $^{87}\text{Sr}/^{86}\text{Sr}$ composition of Neoproterozoic seawater. *Palaeogeogr. Palaeoclimatol. Palaeoecol.* 256, 103–129. <https://doi.org/10.1016/j.palaeo.2007.02.028>.
- Hanshaw, B.B., Back, W., Deike, R.G., 1971. A geochemical hypothesis for dolomitization by ground water. *Econ. Geol.* 66, 710–724. <https://doi.org/10.2113/gsecongeo.66.5.710>.
- Hiatt, E., Pufahl, P., 2014. Cathodoluminescence petrography of carbonate rocks: a review of applications for understanding diagenesis, reservoir quality, and pore system evolution. In: Coulson, I.M. (Ed.), *Cathodoluminescence and its Application to Geoscience*, vol. 45. Mineralogical Association of Canada Short Course, pp. 75–96.
- Higgins, J.A., Schrag, D.P., 2010. Constraining magnesium cycling in marine sediments using magnesium isotopes. *Geochim. Cosmochim. Acta* 74, 5039–5053. <https://doi.org/10.1016/j.gca.2010.05.019>.
- Higgins, J.A., Schrag, D.P., 2012. Records of Neogene seawater chemistry and diagenesis in deep-sea carbonate sediments and pore fluids. *Earth Planet. Sci. Lett.* 357–358, 386–396. <https://doi.org/10.1016/j.epsl.2012.08.030>.
- Hippler, D., Buhl, D., Witbaard, R., Richter, D.K., Immenhauser, A., 2009. Towards a better understanding of magnesium-isotope ratios from marine skeletal carbonates. *Geochim. Cosmochim. Acta* 73, 6134–6146. <https://doi.org/10.1016/j.gca.2009.07.031>.
- Hong, M., Xu, J., Teng, H.H., 2016. Evolution of calcite growth morphology in the presence of magnesium: Implications for the dolomite problem. *Geochim. Cosmochim. Acta* 172, 55–64. <https://doi.org/10.1016/j.gca.2015.09.022>.
- Hu, Z.Y., et al., 2017. Resetting of Mg isotopes between calcite and dolomite during burial metamorphism: Outlook of Mg isotopes as geothermometer and seawater proxy. *Geochim. Cosmochim. Acta* 208, 24–40. <https://doi.org/10.1016/j.gca.2017.03.026>.
- Huang, K.J., et al., 2015. Magnesium isotopic compositions of the Mesoproterozoic dolostones: Implications for Mg isotopic systematics of marine carbonates. *Geochim. Cosmochim. Acta* 164, 333–351. <https://doi.org/10.1016/j.gca.2015.05.002>.
- Immenhauser, A., et al., 2010. Magnesium-isotope fractionation during low-Mg calcite precipitation in a limestone cave – Field study and experiments. *Geochim. Cosmochim. Acta* 74, 4346–4364. <https://doi.org/10.1016/j.gca.2010.05.006>.
- Jacobsen, S.B., Kaufman, A.J., 1999. The Sr, C and O isotopic evolution of Neoproterozoic seawater. *Chem. Geol.* 161, 37–57. [https://doi.org/10.1016/S0009-2541\(99\)00080-7](https://doi.org/10.1016/S0009-2541(99)00080-7).
- Jacobson, A.D., Zhang, Z., Lundstrom, C., Huang, F., 2010. Behavior of Mg isotopes during dedolomitization in the Madison Aquifer, South Dakota. *Earth Planet. Sci. Lett.* 297, 446–452. <https://doi.org/10.1016/j.epsl.2010.06.038>.
- Jones, B., 2005. Dolomite crystal architecture: genetic implications for the origin of the tertiary dolostones of the Cayman Islands. *J. Sediment. Res.* 75, 177–189. <https://doi.org/10.2110/jsr.2005.014>.
- Jones, B., 2013. Microarchitecture of dolomite crystals as revealed by subtle variations in solubility: implications for dolomitization. *Sediment. Geol.* 288, 66–80. <https://doi.org/10.1016/j.sedgeo.2013.01.004>.
- Kaczmarek, S.E., Sibley, D.F., 2011. On the evolution of dolomite stoichiometry and cation order during high-temperature synthesis experiments: an alternative model for the geochemical evolution of natural dolomites. *Sediment. Geol.* 240, 30–40. <https://doi.org/10.1016/j.sedgeo.2011.07.003>.
- Ke, S., et al., 2016. Mg, Sr, and O isotope geochemistry of syenites from northwest Xinjiang, China: Tracing carbonate recycling during Tethyan oceanic subduction. *Chem. Geol.* 437, 109–119. <https://doi.org/10.1016/j.chemgeo.2016.05.002>.
- Knauth, L.P., Kennedy, M.J., 2009. The late Precambrian greening of the Earth. *Nature* 460, 728–732. <https://doi.org/10.1038/nature08213>.
- Land, L.S., 1980. The isotopic and trace element geochemistry of dolomite: the state of the art. In: Zenger, D.H., Dunham, J.B., Ethington, R.L. (Eds.), *Concepts and Models of Dolomitization*. SEPM Society for Sedimentary Geology, Tulsa, OK, pp. 459–477.
- Land, L.S., 1998. Failure to Precipitate Dolomite at 25 °C from Dilute solution despite 1000-Fold Oversaturation after 32 years. *Aquat. Geochem.* 4, 361–368. <https://doi.org/10.1023/A:1009688315854>.
- Last, F.M., Last, W.M., Halden, N.M., 2012. Modern and late Holocene dolomite formation: Manitou Lake, Saskatchewan, Canada. *Sediment. Geol.* 281, 222–237. <https://doi.org/10.1016/j.sedgeo.2012.09.012>.
- Lavoie, D., Jackson, S., Girard, I., 2014. Magnesium isotopes in high-temperature saddle dolomite cements in the lower Paleozoic of Canada. *Sediment. Geol.* 305, 58–68. <https://doi.org/10.1016/j.sedgeo.2014.03.002>.
- Li, F.B., et al., 2016. Constraining ribbon rock dolomitization by Mg isotopes: Implications for the ‘dolomite problem’. *Chem. Geol.* 445, 208–220. <https://doi.org/10.1016/j.chemgeo.2016.06.003>.
- Li, Q., Zhang, Y., Dong, L., Guo, Z., 2018. Oligocene syndepositional lacustrine dolomite: a study from the southern Junggar Basin, NW China. *Palaeogeogr. Palaeoclimatol. Palaeoecol.* 503, 69–80. <https://doi.org/10.1016/j.palaeo.2018.04.004>.
- Li, W.Q., Chakraborty, S., Beard, B.L., Romanek, C.S., Johnson, C.M., 2012. Magnesium isotope fractionation during precipitation of inorganic calcite under laboratory conditions. *Earth Planet. Sci. Lett.* 333–334, 304–316. <https://doi.org/10.1016/j.epsl.2012.04.010>.
- Li, W.Q., Beard, B.L., Li, C.X., Xu, H.F., Johnson, C.M., 2015. Experimental calibration of Mg isotope fractionation between dolomite and aqueous solution and its geological implications. *Geochim. Cosmochim. Acta* 157, 164–181. <https://doi.org/10.1016/j.gca.2015.02.024>.
- Li, W.Y., et al., 2010. Heterogeneous magnesium isotopic composition of the upper continental crust. *Geochim. Cosmochim. Acta* 74, 6867–6884. <https://doi.org/10.1016/j.gca.2010.08.030>.
- Ling, M.X., et al., 2011. Homogeneous magnesium isotopic composition of seawater: an excellent geostandard for Mg isotope analysis. *Rapid Commun. Mass Spectrom.* 25, 2828–2836.
- Lippmann, F., 1982. Stable and metastable solubility diagrams for the system $\text{CaCO}_3\text{-MgCO}_3\text{-H}_2\text{O}$ at ordinary temperatures. *Bull. Mineral.* 105, 273–279.

- Liu, B., 1999. Tectono-sedimentary evolution of north China plate in early paleozoic. *Sci. Geol. Sin.* 34, 347–356.
- Lumsden, D.N., Caudle, G.C., 2001. Origin of massive dolostone: the Upper Knox model. *J. Sediment. Res.* 71, 400–409. <https://doi.org/10.1306/2dc4094e-0e47-11d7-8643000102c1865d>.
- Machel, 2004. Concepts and models of dolomitization: a critical reappraisal. In: Braithwaite, C.J.R., Rizzi, G., Darke, G. (Eds.), *The Geometry and Petrogenesis of Dolomite Hydrocarbon Reservoir*. Geological Society, Special Publications, London, UK, pp. 7–63.
- Machel, H.G., 1985. Cathodoluminescence in calcite and dolomite and its chemical interpretation. *Geosci. Can.* 12, 139–147. <https://journals.lib.umb.ca/index.php/GC/article/view/3427>.
- Markham, G.D., Glusker, J.P., Bock, C.W., 2002. The arrangement of first- and second-sphere water molecules in divalent magnesium complexes: results from molecular orbital and density functional theory and from structural crystallography. *J. Phys. Chem. B* 106, 5118–5134. <https://doi.org/10.1021/jp020078x>.
- Mavromatis, V., Gautier, Q., Bosc, O., Schott, J., 2013. Kinetics of Mg partition and Mg stable isotope fractionation during its incorporation in calcite. *Geochim. Cosmochim. Acta* 114, 188–203. <https://doi.org/10.1016/j.gca.2013.03.024>.
- Mavromatis, V., Meister, P., Oelkers, E.H., 2014. Using stable Mg isotopes to distinguish dolomite formation mechanisms: a case study from the Peru Margin. *Chem. Geol.* 385, 84–91. <https://doi.org/10.1016/j.chemgeo.2014.07.019>.
- Mazzullo, S.J., 1992. Geochemical and neomorphic alteration of dolomite: a review. *Carbonates Evaporites* 7, 21. <https://doi.org/10.1007/BF03175390>.
- Mazzullo, S.J., Chilingarian, G.V., 1996. Dolomite reservoirs: Geochemical techniques for evaluating origin and distribution: by J.R. Allen and W.D. Wiggins. American Association of Petroleum Geologists, 1993, continuing Education Course note Series no. 36. *J. Pet. Sci. Eng.* 14, 262–263. [https://doi.org/10.1016/0920-4105\(95\)00034-8](https://doi.org/10.1016/0920-4105(95)00034-8).
- McKenzie, J.A., 1981. Holocene dolomitization of calcium carbonate sediments from the coastal Sabkhas of Abu Dhabi, U.A.E.: a stable isotope study. *J. Geol.* 89, 185–198. <https://www.jstor.org/stable/30078285>.
- Mresah, M.H., 1998. The massive dolomitization of platformal and basinal sequence-soproposed models from the Paleocene, Northeast Sirte Basin, Libya. *Sediment. Geol.* 116, 199–226. [https://doi.org/10.1016/S0037-0738\(97\)00107-3](https://doi.org/10.1016/S0037-0738(97)00107-3).
- Olanipekun, B.-J., Azmy, K., Brand, U., 2014. Dolomites of the boat harbour formation in the northern peninsula, western Newfoundland, Canada: implications for dolomitization history and porosity control dolomites of the boat harbour formation, northern peninsula, Newfoundland. *AAPG Bull.* 98, 765–791. <https://doi.org/10.1306/08281312141>.
- Peng, Y., et al., 2016. Constraining dolomitization by Mg isotopes: a case study from partially dolomitized limestones of the middle Cambrian Xuzhuang Formation, North China. *Geochem. Geophys. Geosyst.* 17, 1109–1129. <https://doi.org/10.1002/2015GC006057>.
- Perez-Fernandez, A., Berninger, U.N., Mavromatis, V., Pogge von Strandmann, P.A.E., Oelkers, E.H., 2017. Ca and Mg isotope fractionation during the stoichiometric dissolution of dolomite at temperatures from 51 to 126°C and 5bars CO₂ pressure. *Chem. Geol.* 467, 76–88. <https://doi.org/10.1016/j.chemgeo.2017.07.026>.
- Petrasch, D.A., et al., 2017. Microbially catalyzed dolomite formation: from near-surface to burial. *Earth Sci. Rev.* 171, 558–582.
- Pogge von Strandmann, P., Forshaw, J., Schmidt, D., 2014. Modern and Cenozoic records of seawater magnesium from foraminiferal Mg isotopes. *Biogeosciences* 11, 5155–5168. <https://doi.org/10.5194/bg-11-5155-2014>.
- Purser, B., Tucker, M., Zenger, D., 1994. Problems, progress and future research concerning dolomites and dolomitization. In: Purser, B., Tucker, M., Zenger, D. (Eds.), *Dolomites: A Volume in Honour of Dolomieu*. Blackwell Scientific Publications, Cambridge, UK, pp. 1–20.
- Rankey, E.C., 2002. Spatial patterns of sediment accumulation on a holocene carbonate tidal flat, northwest Andros Island, Bahamas. *J. Sediment. Res.* 72, 591–601. <https://doi.org/10.1306/020702720591>.
- Sachan, H.K., 1993. Early-replacement dolomitization and deep-burial modification and stabilization: a case study from the late precambrian of the Zawar area, Rajasthan (India). *Carbonates Evaporites* 8, 191–198. <https://doi.org/10.1007/BF03175177>.
- Saulnier, S., Rollion-Bard, C., Vigier, N., Chaussidon, M., 2012. Mg isotope fractionation during calcite precipitation: an experimental study. *Geochim. Cosmochim. Acta* 91, 75–91. <https://doi.org/10.1016/j.gca.2012.05.024>.
- Schott, J., Mavromatis, V., Fujii, T., Pearce, C.R., Oelkers, E.H., 2016. The control of carbonaceous mineral Mg isotope composition by aqueous speciation: Theoretical and experimental modeling. *Chem. Geol.* 445, 120–134. <https://doi.org/10.1016/j.chemgeo.2016.03.011>.
- Shen, B., Wimpenny, J., Lee, C.T.A., Tollstrup, D., Yin, Q.Z., 2013. Magnesium isotope systematics of endokarst: implications for wallrock reaction in magma chambers. *Chem. Geol.* 356, 209–214. <https://doi.org/10.1016/j.chemgeo.2013.08.018>.
- Shinn, E.A., 1965. Recent Supratidal Dolomite from Andros Island Bahamas. Special Publications of Sepm. <https://doi.org/10.2110/pec.65.07.0112>.
- Siah, M., Hofmann, A., Master, S., Wilson, A., Mayr, C., 2018. Trace element and stable (C, O) and radiogenic (Sr) isotope geochemistry of stromatolitic carbonate rocks of the Mesoarchean Pongola Supergroup: Implications for seawater composition. *Chem. Geol.* 476, 389–406. <https://doi.org/10.1016/j.chemgeo.2017.11.036>.
- Sibley, D.F., 1991. Secular changes in the amount and texture of dolomite. *Geology* 19, 151–154. [https://doi.org/10.1130/0091-7613\(1991\)019<0151:SCITAA>2.3.CO;2](https://doi.org/10.1130/0091-7613(1991)019<0151:SCITAA>2.3.CO;2).
- Sibley, D.F., Gregg, J.M., 1987. Classification of Dolomite Rock Textures. *J. Sediment. Res.* 57, 967–975. <https://doi.org/10.1306/212F8CBA-2B24-11D7-8648000102C1865D>.
- Sibley, D.F., Gregg, J.M., Brown, R.G., Laudon, P.R., 1993. Dolomite crystal size distribution. In: Rezak, R., Lavoie, D.L. (Eds.), *Carbonate Microfabrics*. Springer New York, New York, pp. 195–204.
- Slaughter, M., Hill, R.J., 1991. The influence of organic matter in organogenic dolomitization. *J. Sediment. Res.* 61, 296–303.
- Taylor, T.R., Sibley, D.F., 1986. Petrographic and geochemical characteristics of dolomite types and the origin of ferroan dolomite in the Trenton Formation, Ordovician, Michigan Basin, U.S.A. *Sedimentology* 33, 61–86. <https://doi.org/10.1111/j.1365-3091.1986.tb00745.x>.
- Teng, F.Z., 2017. Magnesia Isotope Geochemistry. *Rev. Mineral. Geochem.* 82, 219–287. <https://doi.org/10.2138/rmg.2017.82.7>.
- Teng, F.Z., Yang, W., 2014. Comparison of factors affecting the accuracy of high-precision magnesium isotope analysis by multi-collector inductively coupled plasma mass spectrometry. *Rapid Commun. Mass Spectrom.* 28, 19–24. <https://doi.org/10.1002/rcm.6752>.
- Tian, S., Zhang, Y., 1997. Ordovician outcrop sequence-stratigraphy in northern north China platform. *Acta Geosci. Sin.* 18, 87–97.
- Tipper, E., et al., 2006. The magnesium isotope budget of the modern ocean: constraints from riverine magnesium isotope ratios. *Earth Planet. Sci. Lett.* 250, 241–253. <https://doi.org/10.1016/j.epsl.2006.07.037>.
- Tipper, E.T., Gaillardet, J., Louvat, P., Capmas, F., White, A.F., 2010. Mg isotope constraints on soil pore-fluid chemistry: evidence from Santa Cruz, California. *Geochim. Cosmochim. Acta* 74, 3883–3896. <https://doi.org/10.1016/j.gca.2010.04.021>.
- Tucker, M.E., Wright, V.P., 2009. *Carbonate sedimentology*. Blackwell Scientific, Oxford, UK, pp. 401–402.
- Wan, S.M., et al., 2017. Enhanced silicate weathering of tropical shelf sediments exposed during glacial lowstands: a sink for atmospheric CO₂. *Geochim. Cosmochim. Acta* 200, 123–144. <https://doi.org/10.1016/j.gca.2016.12.010>.
- Wang, W.Z., et al., 2017. Concentration effect on equilibrium fractionation of Mg-Ca isotopes in carbonate minerals: insights from first-principles calculations. *Geochim. Cosmochim. Acta* 208. <https://doi.org/10.1016/j.gca.2017.03.023>.
- Warren, J., 2000. Dolomite occurrence, evolution and economically important associations. *Earth Sci. Rev.* 52, 1–81. [https://doi.org/10.1016/S0012-8252\(00\)00022-2](https://doi.org/10.1016/S0012-8252(00)00022-2).
- Webb, G.E., Nothdurft, L.D., Kamber, B.S., Klopprogge, J.T., Zhao, J.X., 2009. Rare earth element geochemistry of scleractinian coral skeleton during meteoric diagenesis: a sequence through neomorphism of aragonite to calcite. *Sedimentology* 56, 1433–1463. <https://doi.org/10.1111/j.1365-3091.2008.01041.x>.
- Westphal, H., Munnecke, A., Böhm, F., Bornholdt, S., 2008. Limestone–marl alternations in epeiric sea settings – witnesses of environmental changes or diagenesis? In: Holmden, C., Pratt, B.R. (Eds.), *Dynamics of Epeiric Seas: Sedimentological, Paleontological and Geochemical Perspectives*. Geological Association of Canada Special Paper, Canada, pp. 389–406.
- Wimpenny, J., Colla, C.A., Yin, Q.Z., Rustad, J.R., Casey, W.H., 2014. Investigating the behaviour of Mg isotopes during the formation of clay minerals. *Geochim. Cosmochim. Acta* 128, 178–194. <https://doi.org/10.1016/j.gca.2013.12.012>.
- Winkelstern, I.Z., Lohmann, K.C., 2016. Shallow burial alteration of dolomite and limestone clumped isotope geochemistry. *Geology* 44. <https://doi.org/10.1130/G37809.1>.
- Wombacher, F., et al., 2011. Magnesium stable isotope fractionation in marine biogenic calcite and aragonite. *Geochim. Cosmochim. Acta* 75, 5797–5818. <https://doi.org/10.1016/j.gca.2011.07.017>.
- Xiao, S., Knoll, A.H., Kaufman, A.J., Yin, L., Zhang, Y., 1997. Neoproterozoic fossils in Mesoproterozoic rocks? Chronostratigraphic resolution of a biostratigraphic conundrum from the North China Platform. *Precambrian Res.* 84, 197–220. [https://doi.org/10.1016/S0301-9268\(97\)00029-6](https://doi.org/10.1016/S0301-9268(97)00029-6).
- Xie, D., 1991. Lower Paleozoic. In: Tian, B., Jiang, S., Bao, Y. (Eds.), *Regional Geology of Beijing*. Geology Publishing House, Beijing, pp. 119–128.
- Zenger, D.H., Dunham, J.B., Ethington, R.L., 1994. *Concepts and Models of Dolomitization*. vol. 28. SEPM Society for Sedimentary Geology, Tulsa, OK, pp. 285–286.
- Zhang, F., Yan, C., Teng, H.H., Roden, E.E., Xu, H., 2013. In situ AFM observations of Ca-Mg carbonate crystallization catalyzed by dissolved sulfide: Implications for sedimentary dolomite formation. *Geochim. Cosmochim. Acta* 105, 44–55. <https://doi.org/10.1016/j.gca.2012.11.010>.
- Zheng, R., et al., 1994. Genesis of Dolostone of the Feixiang Formation, lower Triassic in the NE Sichuan Basin: Evidences from Rock Structure and Strontium Content and Isotopic Composition. *Acta Petrol. Sin.* 25, 2459–2468.